

1 **Historical reconstruction of subpolar North Atlantic overturning and its relationship to density**

2 Vassil M. Roussenov¹, Richard G. Williams¹, M. Susan Lozier², N. Penny Holliday³ and Doug Smith⁴

3 ¹Department of Earth, Ocean & Ecological Sciences, School of Environmental Sciences, University of
4 Liverpool, Liverpool L69 3GP, UK

5 ²College of Sciences, Georgia Tech, Georgia, USA

6 ³National Oceanography Centre, Southampton, UK

7 ⁴UK Met Office, Exeter, UK

8 Corresponding author: Vassil Roussenov (vassilr@liverpool.ac.uk), Ric Williams (ric@liverpool.ac.uk)

9

10 **Key Points:**

- 11 • Dominant eastern basin contribution to overturning in reconstructions for the subpolar North Atlantic
12 in accord with recent observations
- 13 • Boundary density changes in the Irminger Sea connect to overturning changes over the eastern
14 subpolar basin
- 15 • Localised buoyancy forcing over the Labrador Sea only enhances the overturning changes over the
16 western side of the subpolar basin

17

18 **Abstract**

19 The connections between the overturning of the subpolar North Atlantic and regional density changes are
20 assessed on interannual and decadal timescales using historical, data-based reconstructions of the
21 overturning over the last 60 years and forward model integrations with buoyancy and wind forcing. The
22 data-based reconstructions reveal a dominant eastern basin contribution to the subpolar overturning in
23 density space and changes in the overturning reaching ± 2.5 Sv, which are both in accord with the
24 Overturning in the Subpolar North Atlantic Program (OSNAP). The zonally-integrated geostrophic velocity
25 across the basin is connected to boundary contrasts in Montgomery potential in density space. The
26 overturning for the eastern side of the basin is strongly correlated with density changes in the Irminger and
27 Labrador Seas, while the overturning for the western side is correlated with boundary density changes in
28 the Labrador Sea. These boundary density signals are a consequence of local atmospheric forcing and
29 transport of upstream density changes. In forward model experiments, a localised density increase over the
30 Irminger Sea increases the overturning over both sides of the basin due to dense waters spreading to the
31 Labrador Sea. Conversely, a localised density increase over the Labrador Sea only increases the
32 overturning for the western basin and instead eventually decreases the overturning for the eastern basin.
33 Labrador Sea density provides a useful overturning metric by its direct control of the overturning over the
34 western side and lower latitudes of the subpolar basin.

36 **Plain Language Summary**

37 The overturning in the subpolar North Atlantic is reconstructed from historical data over the last 60 years.
38 These reconstructions are consistent with ongoing observational measurements confirming that the
39 overturning is dominated by an eastern basin contribution from between Greenland and Scotland. This
40 overturning response is strongly correlated with density changes in the Labrador Sea and Irminger Seas.
41 The boundary density for the Irminger Sea provides a direct control of the overturning over the eastern side
42 of the basin and similarly the boundary density around the Labrador Sea directly affects the overturning
43 over the western side of the basin. Model experiments are conducted using localised forcing, showing that
44 a density increase over the Irminger Sea enhances the overturning over the entire basin, while a density
45 increase over the Labrador Sea instead eventually decreases the overturning for the eastern basin through
46 a southern influx of warmer and lighter water.

1 Introduction

There is a widespread view that the meridional overturning in the subpolar North Atlantic is determined by processes acting within the Labrador Sea (Delworth et al., 1993; Eden and Willebrand, 2001) with the strength of the overturning associated with density changes in the Labrador Sea (Robson et al., 2014a and 2016; Ortega et al., 2017). However, continuous observations of the overturning in density space from the Overturning in the Subpolar North Atlantic Program (OSNAP, Lozier et al., 2017) have recently challenged this viewpoint of a dominant Labrador Sea contribution, by revealing an overturning contribution that is much larger over the eastern side of the subpolar basin, compared with the western contribution (Lozier et al., 2019; Li et al., 2021). There is a question of how to reconcile these two perspectives.

The inferences from the OSNAP observational program are based so far on 4 years of continuous observations (Li et al., 2021), so there is a practical issue of how representative the OSNAP findings are for longer periods. In addition, there is a question as to how the subpolar overturning connects to the regional density distribution, including over the Labrador Sea, the Irminger Sea and the Iceland Basin. The regional connections between the subpolar overturning and regional density changes may be due to a combination of the local imprint of the atmospheric forcing, associated with the North Atlantic Oscillation (Robson et al., 2014a), and/or through the gyre-scale redistribution of upstream density anomalies (Menary et al., 2020).

In this study, data-based reconstructions of the annual overturning in density co-ordinates are used to assess how representative the OSNAP analyses of four years of monthly overturning is in time and space (Section 2). The historical analyses provide an annual context for the overturning over the last 60 years, as well as a comparison between the meridional overturning across latitude circles. The zonally-integrated geostrophic velocity across the basin is connected to boundary contrasts in Montgomery potential along density surfaces for different composites of the North Atlantic Oscillation (NAO). The data-based reconstructions reveal how the western and eastern contributions to OSNAP overturning correlate with regional density changes. Forward model integrations are then performed (Section 3) to identify how regional density changes and associated overturning signals are induced by localised buoyancy and wind forcing patterns associated with the NAO. This combination of historical data reconstruction and forward model integrations is then used to test the extent to which the Labrador Sea density provides a useful metric of how the subpolar overturning varies (Li et al., 2019) and the implicit causality contained within this relationship (Section 4).

2 Data-based reconstructions of the overturning

2.1 Methods

In order to address how representative, the OSNAP measurements are, we estimate the overturning from historical temperature and salinity data assimilated into a dynamical model (Williams et al., 2014, 2015), similar to previous diagnostic studies for the North Atlantic (Mellor et al, 1982; Greatbatch et al., 1991):

- i. Historical temperature and salinity changes are obtained from the Met Office statistical ocean reanalysis (MOSORA, Smith et al. 2015). This is a global optimal interpolation of the available hydrographic data and recent Argo data from 1950 to 2020 with a horizontal resolution of 1.25° and with 20 vertical levels. Data sparse regions are filled by extrapolating from the observational data using covariances from a perturbed

86 physics ensemble of the Hadley Centre model (HadCM3) and then iteratively updated with observations
87 (Smith et al., 2015).

88 ii. The global MIT general circulation model (Marshall et al., 1997) is initialized with the annual mean
89 temperature and salinity data based on monthly means from Hadley Centre analyses of temperature and
90 salinity data, interpolating the slightly coarser historical data analyses onto a 1° grid with 23 vertical levels
91 over the globe. This global MIT model is integrated forward with an initial 1-month spin up and then a
92 further 12 months to cover an annual cycle. This dynamical adjustment allows the circulation to spin up that
93 is dynamical consistent with the density distribution. The model includes forcing from monthly-mean wind
94 stresses from ECMWF for each year (using ERA40 for years 1960 to 1978 and ERA Interim for 1979 to
95 2020), so including the Ekman contribution to the overturning. The dynamical adjustment does not include
96 explicit surface heat or freshwater fluxes, but includes a weak artificial relaxation of temperature and salinity
97 to the initial annual-averaged temperature and salinity data on a timescale of 36 months, which acts to
98 minimise model drift. The effect of the mesoscale eddy transport is taken into account by using the Gent
99 and McWilliams (1990) sub-grid scale mixing parameterization.

100 iii. This initialisation and assimilation procedure is repeated for each separate year from 1960 to 2020. The
101 subsequent changes in overturning are then evaluated from these dynamically-adjusted velocities and
102 densities covering an annual cycle.

103

104 This dynamical assimilation approach avoids the difficulty of model drift that occurs with integrations over
105 several decades and by design the overturning circulation is dynamically consistent with the density
106 distribution. There are two important caveats to this procedure: firstly, the assimilated products only
107 provide annual estimates of the overturning, so omit seasonal variability, and secondly they are based on a
108 dynamical assimilation on a 1° grid, so omit dynamical effects of finer-scale mesoscale circulations. Despite
109 these caveats, this approach has proven useful in assessing decadal changes in ocean basin-scale
110 overturning and heat content (Lozier et al., 2010; Williams et al., 2014 and 2015); see model tests of our
111 approach comparing our density-based reconstructions of the overturning and the actual model overturning
112 from GECCO for two twenty year periods (Lozier et al., 2010) and from ECCO for two five year periods
113 (Williams et al., 2014). Our dynamical assimilation approach is the same as reported in Williams et al.
114 (2015), apart from including additional years of data input.

115

116 The overturning is calculated in density coordinates, as there are strongly sloping density surfaces across
117 the subpolar basin (Holliday et al., 2018) that complicate the interpretation of the overturning in depth
118 space. The overturning in density space naturally combines the overturning in depth space and the
119 horizontal gyre circulation together. The overturning streamfunction, $\psi(\sigma)$ in Sv, is estimated in density
120 space following the OSNAP programme (Lozier et al., 2019; Li et al., 2021) by

$$121 \quad \psi(\sigma) = - \int_{s_w}^{s_e} \int_{\sigma_{max}}^{\sigma_{min}} V_{\perp}(s, \sigma) d\sigma ds, \quad (1)$$

122 where s_e and s_w are the eastern and western ends of the section with s measuring the distance along the
123 section (with positive in the eastward direction), σ_{min} and σ_{max} are the minimum and maximum potential
124 densities for the overturning, the potential density is referenced to the sea surface, and $V_{\perp}(s, \sigma)$ is the
125 volume flux per unit length per unit density normal to the section (with a northward component taken to be

positive). The minimum density is always the lightest density along the section and the maximum density may either be chosen to be fixed or is the density that provides the maximum value of the overturning streamfunction. The estimate of the overturning in density space from the OSNAP field programme is only marginally changed when calculated using neutral densities (Lozier et al., 2019).

Observational arrays are designed to monitor the overturning in the Atlantic (McCarthy et al., 2020) across a coast to coast section by calculating the Ekman transport from atmospheric wind-stress and measuring the geostrophic shear and bottom velocity or external model, and ensuring an overall mass balance (Baehr et al., 2004; Hirschi and Marotzke, 2007; Li et al., 2017).

The variability of the overturning on annual timescales and longer is dominated by the geostrophic shear contributions (Hirschi and Marotzke, 2007), which has led to the focus on boundary end point monitoring of the density contributing to the overturning circulation. In cartesian co-ordinates, the zonal integral of the meridional geostrophic velocity, $v_g = \frac{1}{\rho f} \frac{\partial P}{\partial x} \Big|_z$, across a basin is simply given by the east-west boundary contrasts in pressure at the same depth (Marotzke et al., 1999),

$$\int_{x_w}^{x_e} v_g(x, z) dx = \frac{1}{\rho f} (P_e - P_w), \quad (2)$$

where ρ is a reference density, f is the Coriolis parameter, P_e and P_w are the pressures on the eastern and western boundaries. The boundary pressures are themselves connected to the boundary densities via the hydrostatic balance.

For the subpolar gyre, a density-based view of the overturning is more appropriate than a depth-based view. Drawing upon how the geostrophic flow varies along isentropic surfaces in the atmosphere (Montgomery, 1937), the meridional geostrophic velocity, v_g , is connected to horizontal gradients of the Montgomery potential (m^2s^{-2}) where $M = \alpha P + gz$ (Bleck and Smith, 1990), and α is the specific volume anomaly, P is pressure and z is the depth of the specific volume anomaly surface. The Montgomery potential provides a geostrophic streamline along a specific volume surface,

$$v_g = \frac{1}{f} \frac{\partial M}{\partial x} \Big|_{\alpha},$$

so that the zonal integral of the meridional geostrophic velocity across a basin is then given by the east-west boundary contrasts in Montgomery potential evaluated along the same specific volume surface,

$$\int_{x_w}^{x_e} v_g(x, \alpha) dx = \frac{1}{f} (M_e - M_w)_{\alpha}, \quad (3)$$

and M_e and M_w are the Montgomery potential on the eastern and western boundaries.

As the subpolar overturning in (1) is evaluated in potential density co-ordinates, we choose to connect the geostrophic flow to the Montgomery potential along potential density surfaces referenced to the sea surface as an approximation to specific volume surfaces; this equivalence in using the Montgomery potential is not exact due to non-linearities from the equation of state, including a term due to differences between the pressure on the potential density and the reference sea surface pressure (McDougall and Klocker, 2010). The Montgomery potential, $M = \alpha P + gz$, is evaluated in the following manner: (i) the density is evaluated from the gridded temperature and salinity data using the international thermodynamic equation of state

165 (McDougall *et al.*, 2009); (ii) the density within the water column directly alter the specific volume anomaly
166 α and the height of the potential density surface, z ; (iii) the pressure P is made up of a sea surface height
167 contribution and a depth-varying contribution depending upon the density distribution from hydrostatic
168 balance. This calculation of the Montgomery potential is performed for each potential density layer. The
169 potential density surfaces are close to the specific volume surfaces over the upper water column, so that
170 the Montgomery potential then defines the geostrophic flow in density co-ordinates, as applied in an
171 isopycnic circulation model (MICOM, Bleck and Smith, 2012). The zonal integral of the meridional
172 geostrophic velocity across a basin is then given by the east-west boundary contrasts in Montgomery
173 potential evaluated along the same potential density surface,

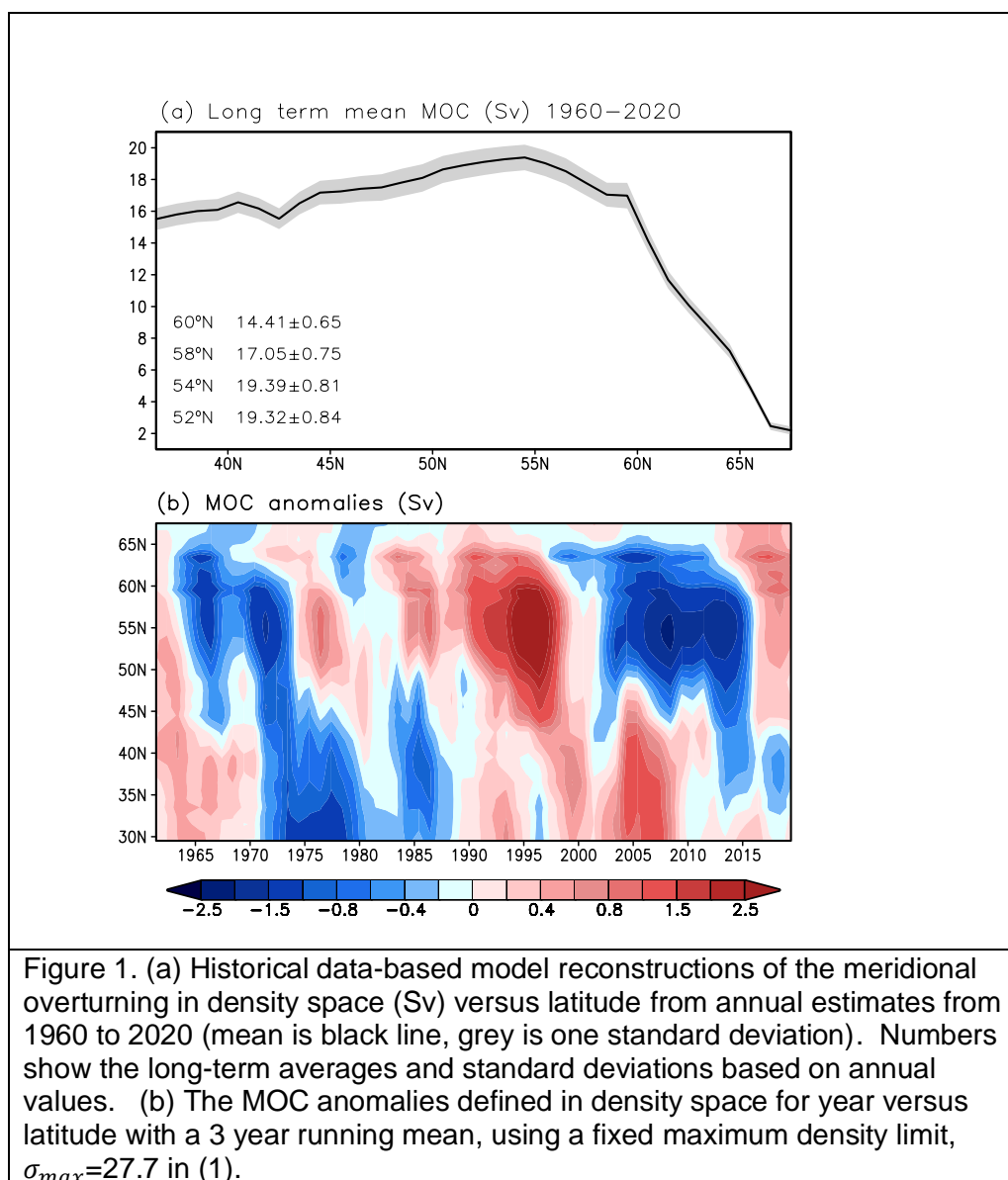
$$\int_{x_w}^{x_e} v_g(x, \sigma) dx = \frac{1}{f} (M_e - M_w) \sigma, \quad (4)$$

175 where σ defines the density surface. If the density surfaces outcrop or ground, then the boundary value of
176 the Montgomery potential within the zonal integral in (4) is taken at the point of the outcrop or grounding
177 point, rather than at the western or eastern boundary. For density surfaces that outcrop, the Montgomery
178 potential is controlled by the surface pressure. This calculation of the Montgomery potential is used to
179 interpret the changes in the velocity structure for potential density surfaces the upper 1 km along the
180 OSNAP sections for both the climate mean and different states of the North Atlantic Oscillation (section
181 2.4).

182 183 *2.2 Historical reconstruction of the overturning over the subpolar gyre*

184
185 Our historical data-based reconstruction of the overturning defined in terms of density using (1) strongly
186 varies over the subpolar latitudes, ranging from a subpolar maximum of 19.39 ± 0.81 Sv at 54°N to
187 14.41 ± 0.65 Sv at 60°N (Fig. 1a). The subpolar anomalies in the density-based overturning reach up to
188 ± 2.5 Sv and are negative for years 1965 to 1970, changing to positive for 1975 to 2000, and returning to
189 negative for 2000 to 2017. This variability in the subpolar overturning in density space compares with a
190 strengthening in the subpolar overturning in depth space of typically 1 Sv during 1980 to 2000 compared
191 with 1950 to 1970 (Lozier *et al.*, 2010). The temporal changes in the meridional overturning from the
192 subtropical gyre to the subpolar gyre leads in the early 1970s to a decrease in northward heat transport and
193 loss in subpolar heat content and an increase northward in the mid 1990s and a gain in subpolar heat
194 content (Williams *et al.*, 2015); see studies revealing this subpolar loss and gain of heat using an ocean
195 model by Robson *et al.* (2012) and analyses of a coupled model prediction system by Robson *et al.*
196 (2014b).

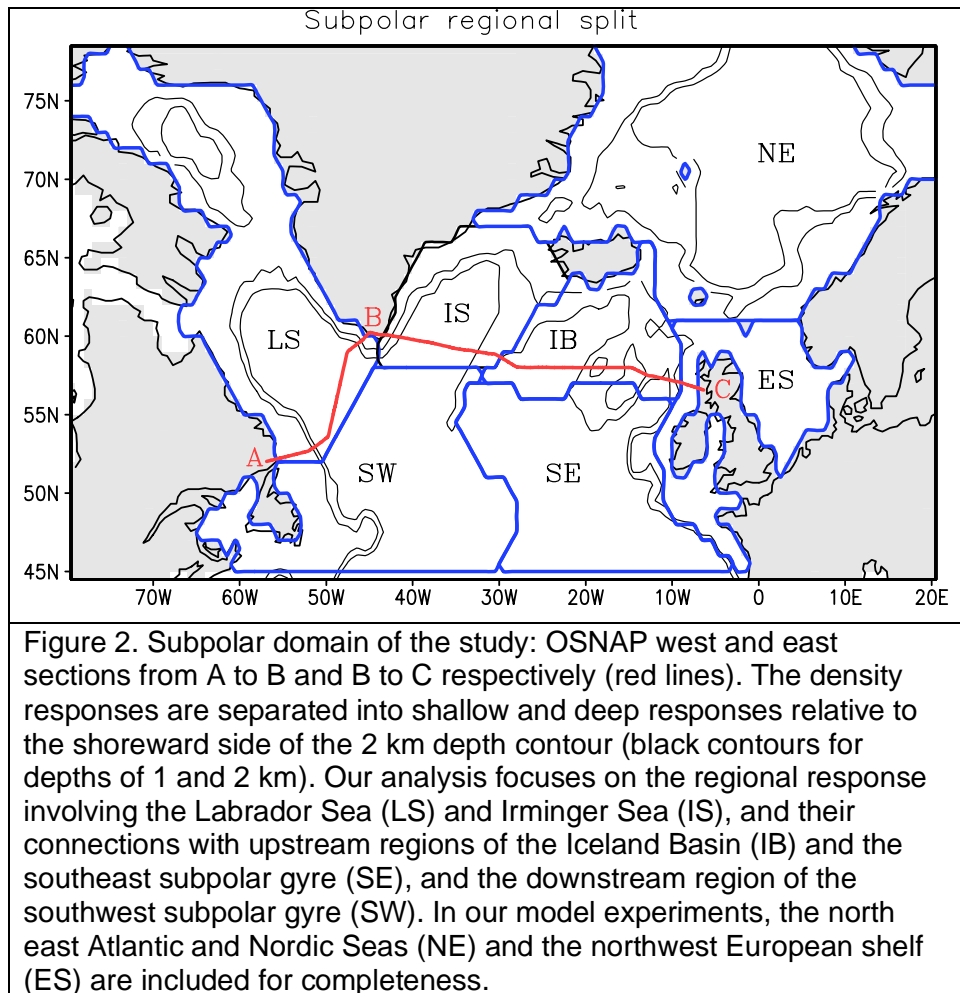
197
198 The changes in the overturning include regions where there appears to be signals propagating southward
199 with latitude from 65°N to 58°N , and regions where there appears to a very coherent response with latitude
200 from 40°N to 58°N (Fig. 1b). The overturning anomalies often have the opposite sign between the
201 subtropical and subpolar gyres. There is often a break in the latitudinal communication between the gyres
202 at around 45°N , as revealed on interannual to decadal timescales in ocean model experiments using
203 cartesian and isopycnal co-ordinates (Bingham *et al.*, 2007; Buckley and Marshall, 2016; Zou *et al.*, 2020).



206

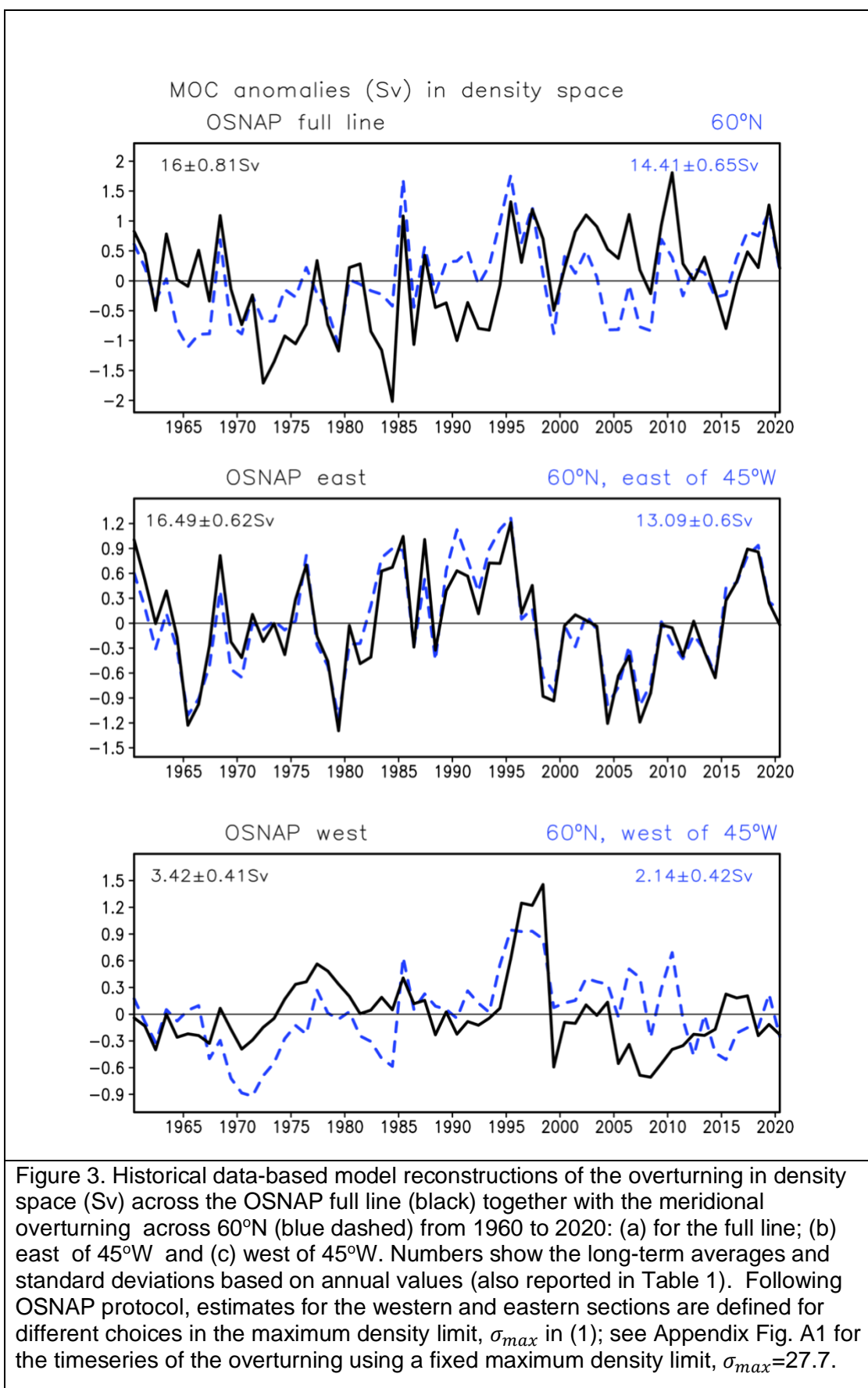
207 Our aim is now to explore the subpolar overturning signals and their connections to boundary density by
 208 focussing on reconstructions for the OSNAP observing system (Lozier et al., 2017). The OSNAP observing
 209 system running coast to coast across the subpolar North Atlantic (Fig. 2) reveals an overturning in density
 210 space with a mean and standard deviation for annual means of 16.6 ± 0.8 Sv over the period 2014 to 2018
 211 (Lozier et al., 2019; Li et al., 2021). The annual standard deviation is reported here rather than the smaller
 212 standard error as the relevant issue is how representative a 4 year snapshot is compared to our 60 year
 213 reconstructions. The overturning is dominated by the contribution from the eastern side of the basin,
 214 OSNAP east, running from the southeastern tip of Greenland to the Scotland shelf, reaching 16.8 ± 1.0 Sv.
 215 The overturning contribution on the western side of the basin, OSNAP west, running from the southwestern
 216 Labrador shelf to the southwestern tip of Greenland, instead only reaches 2.6 ± 0.5 Sv.

217



218
 219
 220
 221
 222
 223
 224
 225
 226
 227
 228
 229
 230
 231

The long-term estimates of the overturning from the data-based reconstructions from 1960 to 2020 (Fig. 3, black line) are consistent with the OSNAP analyses from 2014 to 2018 (Table 1): there is an overturning across the entire section of 16.0 ± 0.8 Sv, with a dominant contribution from the eastern side of the basin of 16.49 ± 0.62 Sv and a weaker contribution on the western side of 3.42 ± 0.41 Sv (where again the mean and standard deviations are reported). The western contribution is larger in the data-based reconstruction than measured in OSNAP, but the difference is within the variability indicated by the standard deviations. In agreement with the observations there is a larger contribution and variability in the overturning for the eastern section than for the western section. When diagnosed for the same period as the OSNAP analyses from 2014 to 2018, the reconstructions for the overturning are only slightly altered (Table 1), reaching 15.94 ± 0.43 Sv across the entire section, 16.86 ± 0.56 Sv on the eastern section and 3.46 ± 0.20 Sv on the western section.



The reconstruction for the overturning is evaluated using a variable maximum density limit, σ_{max} , chosen to maximise the overturning using (1). This maximum density limit, σ_{max} , varies between 27.5 to 27.6 for the eastern section and increases from 27.7 to 27.8 for the western section, and is a compromise of 27.6 to

237 27.7 for the full line. By design, these choices of σ_{max} identify the maximum overturning across an
 238 individual section, but have the deficiency that the overturning crossing the full line is not equal to the sum
 239 of the overturning contributions from the eastern and western sections (Table 1). This mismatch is due to
 240 some of the waters in the lower limb of OSNAP east being further densified in the Labrador Sea (Lozier et
 241 al., 2019), so that their transport contributions appear in different density classes for each section and are
 242 counted twice when summing over both sections.
 243

Table 1. Observational and our data-based modelling estimates of the overturning (Sv) across full line, west and east lines using either a variable or fixed maximum density limit. The overturning is estimated in density space along the model OSNAP line. The mean and standard deviation for annual means are included, as well as characteristic values for different atmospheric states, NAO+ and NAO-.

	full line	west of 45°W	east of 45°W
Observations from OSNAP for 2014 to 2018 using variable density for maximum overturning (using a variable σ_{max}) from Li et al. (2021).	16.6±0.8	2.6±0.5	16.8±1.0
Data-based model reconstruction for 1960 to 2020 using OSNAP protocol for maximum overturning (using a variable σ_{max}).	16.00±0.81	3.42±0.41	16.49±0.62
Data-based model reconstruction for 2014 to 2018 using OSNAP protocol for maximum overturning (using a variable σ_{max}).	15.94±0.43	3.46±0.20	16.86±0.56
Data based reconstruction for 1960 to 2020 for the overturning using a fixed maximum density limit of $\sigma_{max} = 27.6$.	15.95±0.8	0.25±1.5	15.71±1.1
Data based reconstruction for 1960 to 2020 for the overturning using a fixed maximum density limit of $\sigma_{max} = 27.7$.	13.95±1.04	2.71±0.84	11.24±0.88
Overturning response for NAO+ years (Fig. 8a, red for 16 years) for fixed maximum density limit, $\sigma_{max} = 27.7$.	1.56	0.44	1.12
Overturning response for NAO- years (Fig. 8a, blue for 12 years) for fixed maximum density limit, $\sigma_{max} = 27.7$.	-0.55	-0.16	-0.39

244 Alternatively, the overturning may be evaluated using the same maximum density limit, σ_{max} , across all
 245

sections, which leads to reduced estimates of the overturning (Table 1 for σ_{max} of 27.6 or 27.7), but with the overturning across the full line being the sum of the overturning contributions from the western and eastern sections. When the same σ_{max} is chosen, then the variability is comparable from both the western and eastern sections (Fig. A1 for $\sigma_{max} = 27.7$).

2.3 Connections between the overturning across the OSNAP line and the meridional overturning at different latitudes

The reconstruction of the overturning over OSNAP east is strongly correlated with the meridional overturning across 60°N at zero lag (Fig. 3, blue line; Fig. 4, black lines), reaching 0.94 and 0.83 for the eastern section and the full line (Table 2). The overturning for OSNAP east is only weakly correlated with the meridional overturning at latitudes further south than 57°N (Fig. 4a), including timescale lags of up to 6 years, although the correlations do rise if a 3 year smoothing is applied (Fig. 4c). There are high, negative correlations between the overturning at OSNAP east and the meridional overturning in the subtropical gyre at lags from 0 to 3 years. These subtropical signals are likely to be a consequence of the atmospheric forcing in the subtropical gyre that are out of phase with the atmospheric forcing along OSNAP east.

The reconstruction of the overturning over OSNAP west is strongly correlated with the meridional overturning across the western section of 60°N and is also correlated at lower latitudes in the subpolar gyre, reaching 0.93 for the western section, 0.64 for 52°N and 0.51 for 46°N for zero lag (Table 2). Further south at 40°N, there is an increased correlation between OSNAP west with lags for the lower latitude response of 2 to 3 years (Fig. 4b). The lagged correlations between the overturning at OSNAP west and the low latitudes significantly increases if a 3 year smoothing is applied (Fig. 4d). This response within the subpolar gyre is consistent with the overturning signals being communicated southward by an adjustment of boundary density signals.

Table 2. Correlations between overturning for OSNAP east and OSNAP west with the meridional overturning for 60°N, 52°N and 46°N latitude circles. Correlations are zero lag based on historical data based reconstructions for annual estimates using unsmoothed time series from 1960 to 2020. Values of at least 99% confidence of 0.44 are in bold and at 98% confidence of 0.32 in italics.		
OSNAP east	60°N east of 45°W	0.94
	60°N full line	0.83
	52°N full line	0.30
	46°N full line	0.30
OSNAP west	60°N west of 45°W	0.93
	60°N full line	<i>0.41</i>
	52°N full line	0.64
	46°N full line	0.51

There are also low latitude signals where the subtropics are correlating with OSNAP west with a maximum correlation of 0.4 on lagged timescales of 5 years rising to 0.5 for smoothed data (Fig. 5b,d). This subtropical signal does not strongly vary with latitude from 20°N to 35°N and might either reflect an imprint

276 of changing atmospheric forcing or a possible propagating feature from the subpolar gyre. From the
 277 observational data alone, it is difficult to separate these two processes, an ocean internal communication to
 278 far field forcing versus a local response to atmospheric forcing. For example, temporal changes in the
 279 pattern of wind forcing associated with the NAO may give interannual to decadal changes in sea surface
 280 temperature, which are not necessarily advected at the surface, but instead represent a local response to
 281 the time-varying wind forcing (Visbeck et al., 1998) and/or a sub-surface advective pathway (Foukal and
 282 Lozier, 2016). In addition, on multi-decadal timescales, the effect of changes in atmospheric wind forcing
 283 can lead to opposing sign anomalies in the meridional overturning over the subtropical and subpolar gyres
 284 (Lozier et al., 2010; Williams et al., 2014; Zou et al., 2020). This competition of local and far field
 285 responses to atmospheric forcing is explored later in regionally-forced model experiments in Section 3.
 286

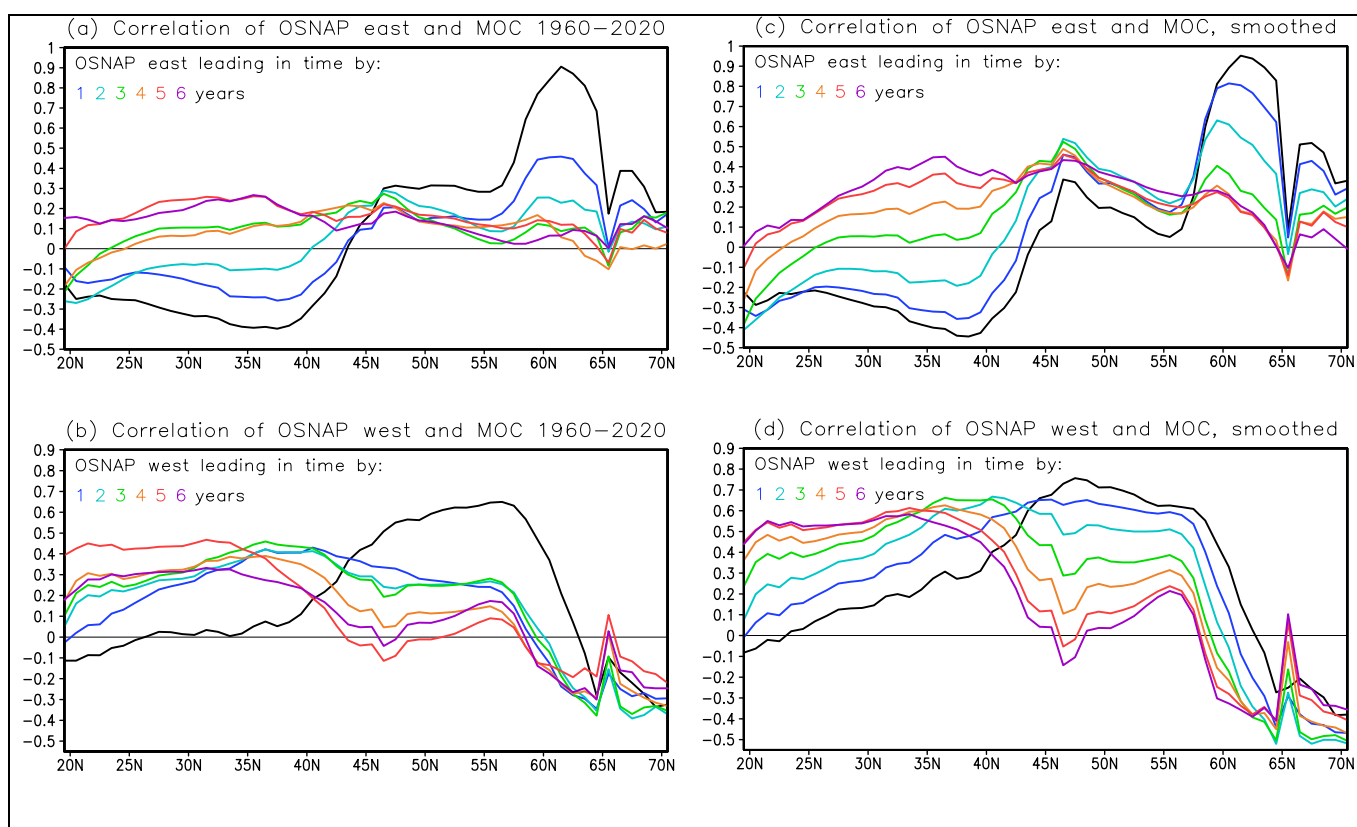


Figure 4. The lagged correlations between annual time series for (a, c) the overturning for OSNAP east and the meridional overturning at each latitude and (b, d) the overturning for OSNAP west and the meridional overturning at each latitude. The lagged correlations are shown both for unsmoothed timeseries (a, b) and with a 3 year smoothing window (c, d). The black line is for zero lag and blue to red lines for lags 1 to 6 years, where a lag denotes a later latitudinal response to the changes on the OSNAP sections.

287
 288 **2.4 Changes in the overturning across the OSNAP lines connected to different states of the North Atlantic**
 289 **Oscillation**

290 The overturning record is assessed in terms of the connection to the North Atlantic Oscillation (NAO), using
 291 a station-based index (Hurrell, 2013) with a magnitude threshold of 1.8 used to define annual composites of
 292 NAO+ states for 16 years and NAO- states for 12 years (Fig. 8a). The overturning across the OSNAP full
 293 line is increased during NAO+ by 1.56 Sv and reduced during NAO- by -0.55 Sv with similarly-signed
 294 changes in the western and eastern sides of the basin (Table 1). Over OSNAP east, there is an increase in

295 the density reaching 0.05 kg m^{-3} over the upper 800m over the western side of the section during NAO+
296 states relative to the climate mean, and conversely there is a similar decrease in the density during NAO-
297 states (Fig. 5a,c,e). The northward geostrophic shear then is enhanced and acts to increase the meridional
298 overturning during NAO+ state, and conversely is decreased during the NAO- states. This response is
299 consistent with subpolar gyre cyclonic circulation being enhanced during NAO+ and weakened during
300 NAO- (as indicated by the anomalous patterns in sea surface height in Fig. A2).

301 In density co-ordinates, the geostrophic flow may be approximated by the boundary contrasts in
302 Montgomery potential along potential density surfaces, where the Montgomery potential, $M = \alpha P + gz$, is
303 determined from the density within the water column and the sea surface height (section 2.1). For OSNAP
304 east in the climate mean, there is a westward decrease in the Montgomery potential along σ surfaces from
305 27.3 to 27.7, which is consistent with a northward geostrophic flow (Fig. 5b). The average geostrophic
306 velocity along the 27.6 surface is northward from (4) due to the Montgomery potential on the western
307 boundary being less than that on the eastern boundary (Fig. 5g). For NAO+ states, the Montgomery
308 potential anomaly decreases westward along σ surfaces from 27.3 to 27.7, implying a stronger northward
309 geostrophic flow and a stronger meridional overturning (Fig. 5d). For NAO- states, the Montgomery
310 potential anomaly increases westward along these σ surfaces from 27.3 to 27.7, implying a weakening in
311 the northward geostrophic flow and a weaker meridional overturning (Fig. 5f). Accordingly, along the 27.6
312 surface, during a NAO+ state, the average northward geostrophic flow is enhanced over the section with a
313 negative Montgomery potential anomaly on the western boundary and conversely the opposing response
314 occurs for a NAO- state (Fig. 5h, blue and red lines).

315 The geostrophic flow responses are more complex over OSNAP west, but can still be understood in terms
316 of the contrasts in Montgomery potential. In the climate mean, there is a north-westward flow over the
317 Greenland side of OSNAP west changing to a south-westward flow over the Labrador side, which
318 corresponds to the Montgomery potential being positive at the southern tip of Greenland, negative over
319 most of the Labrador Sea and either weakly negative for denser surfaces or weakly positive for lighter
320 surfaces over the south-western boundary of the Labrador Sea (Fig. 5b). For NAO+ states, the
321 Montgomery potential anomaly is negative (Fig. 5d, h) with a more negative value on the southwestern end
322 compared with the north-eastern end, implying a slight increase in the north-westward overturning across
323 the section. For NAO- states, the Montgomery potential anomaly is positive (Fig. 5f, h) with a more positive
324 value on the north-eastern end compared with the southwestern end, implying a slight decrease in the
325 north-westward overturning across the section.

326
327 These changes in the Montgomery potential then reveal similar-signed changes in the geostrophic
328 velocities contributing to the overturning for OSNAP west and east with a larger contribution from OSNAP
329 east for both NAO+ and NAO- states, consistent with the volumetric diagnostics in Table 1. The
330 geostrophic contribution to the overturning in Sv may be estimated from the zonal integral of the product of
331 geostrophic velocity and layer thickness, given by $\int_{x_w}^{x_e} v_g(x, \sigma) h(x, \sigma) dx$, where $h(x, \sigma)$ is the layer thickness,
332 varying with longitude and density, and the geostrophic velocity is estimated from the west-east gradient in

333 Montgomery potential, $v_g = (1/f)\partial M/\partial x$. This Montgomery-based estimate of the overturning is 3.21 Sv for
 334 OSNAP west and 16.44 Sv for OSNAP east for a climate mean, very close to the corresponding direct
 335 diagnostics of 3.42 Sv for OSNAP west and 16.49 Sv for OSNAP east in Table 1.
 336

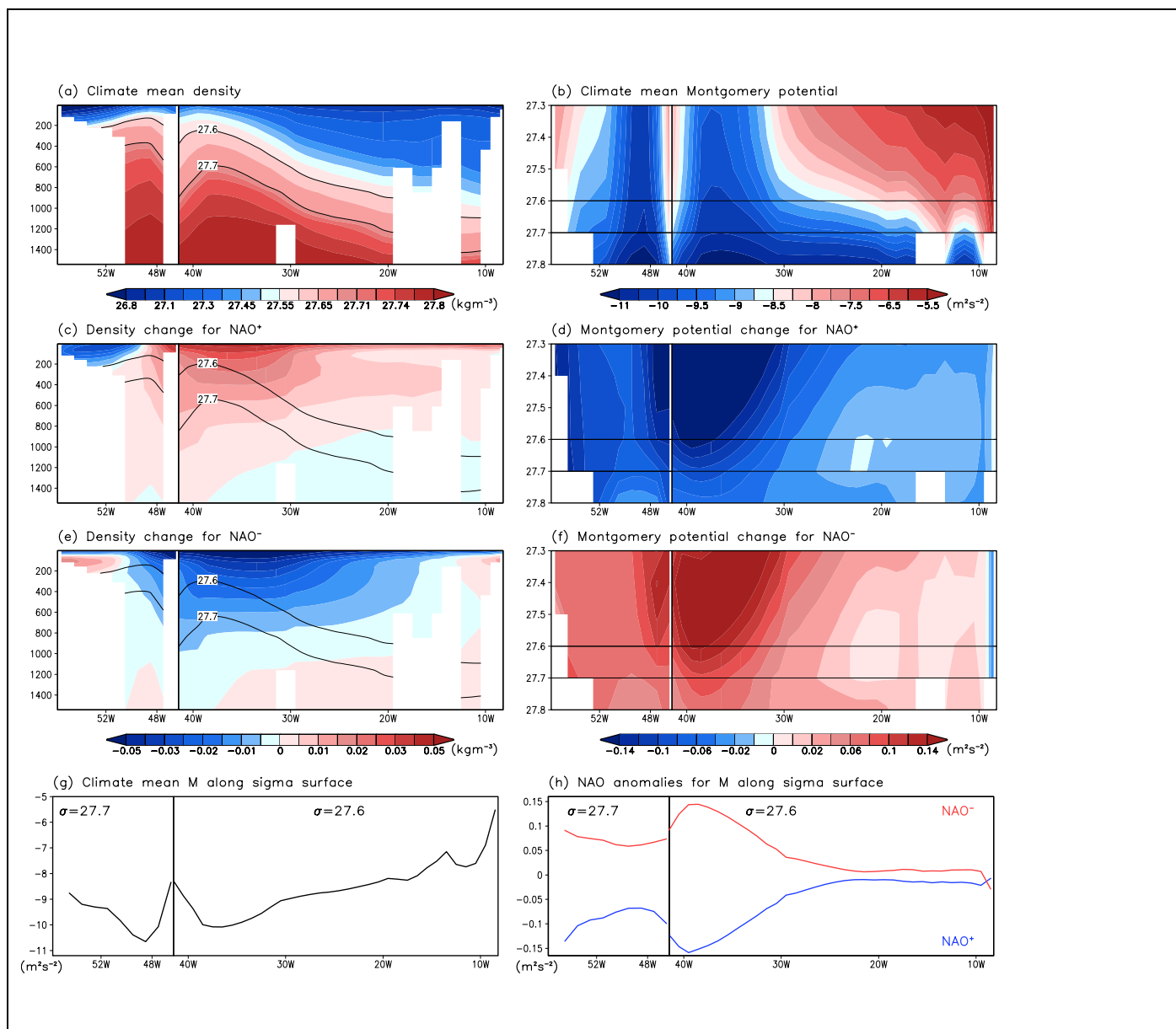


Figure 5. Combined OSNAP west and east sections for potential density σ surfaces (kg m^{-3}) versus depth and Montgomery potential (m^2s^{-2}) versus σ from our data-based diagnostics for a climate mean from years 1960 to 2020 in (a,b), and their anomalies for a composite of NAO+ states in (c,d) and NAO- states in (e,f). The Montgomery potential (m^2s^{-2}) versus longitude along the $\sigma=27.6$ surface for OSNAP east and 27.7 surface for OSNAP west for the climate mean in (g) and the anomalies for the NAO+ (blue line) and NAO- (red line) composites in (h). In panels (a) to (f), the σ surfaces 27.6 and 27.7 surfaces are marked in black.

337

338

339 2.5 Connection between density and the overturning

340

341

342

343

Given the imprint of the atmospheric forcing associated with the NAO states on both the density distribution and the geostrophic circulation (Fig. 5c-f), now consider how the time series for the meridional overturning connects to the density distribution for this data-based reconstruction. In these historical reconstructions, the overturning for OSNAP east correlates with regional density anomalies in the Irminger Sea, with a

344 correlation coefficient ranging from 0.44 on the boundary and 0.56 for the southeast Irminger Sea at zero
345 lag in Table 3. Maps of the correlation between the timeseries for the overturning for OSNAP east and the
346 regional density above the 27.6 surface reveal correlations greater than 0.3 and reaching 0.5 over the
347 Irminger Sea at zero lag and a similar pattern for the meridional overturning across the eastern side of 60°N
348 (Fig. 6a,b). In comparison, Li et al. (2021), using 46 months of monthly OSNAP data obtain a smaller
349 correlation of 0.31 between the OSNAP east overturning and the same overturning metric calculated using
350 variable velocity and density only at the western boundary. This mismatch with our data-based
351 reconstruction is likely due to the timescale of interest, as we are using annual means and the OSNAP
352 record to date is dominated by sub-seasonal variability. Similar to our study, Menary et al. (2020) obtained
353 a correlation of 0.6 using annual model data between the overturning for the eastern side of the basin and
354 the density along the western side of the Irminger Sea.

355

Table 3. Correlations at zero lag between the overturning for OSNAP east and OSNAP west with the regional density above the potential density surfaces σ of 27.6 and 27.7 respectively based on historical data-based reconstructions from 1960 to 2020. The regional density is separated into boundary or interior regions, where the boundary region extends from the coast to the 2000 m isobath. Values of at least 99% confidence of magnitude of 0.44 are in bold and of 98% confidence of magnitude of 0.32 in italics.		
OSNAP east	Iceland Basin	0.51
with density	Irminger Sea boundary	0.44
above 27.6	Irminger Sea interior	0.51
	Southeast Irminger Sea	0.56
	Labrador boundary	-0.23
	Labrador interior	0.07
OSNAP west	Irminger Sea boundary	-0.33
with density	Irminger Sea interior	-0.37
above 27.7	Labrador boundary including western and eastern end of OSNAP west	0.62
	Labrador interior	0.24
	Labrador boundary at western end of OSNAP west	0.53
	Labrador boundary at eastern end of OSNAP west	-0.23
	52°N west boundary	0.47
	46°N west boundary	0.33

356

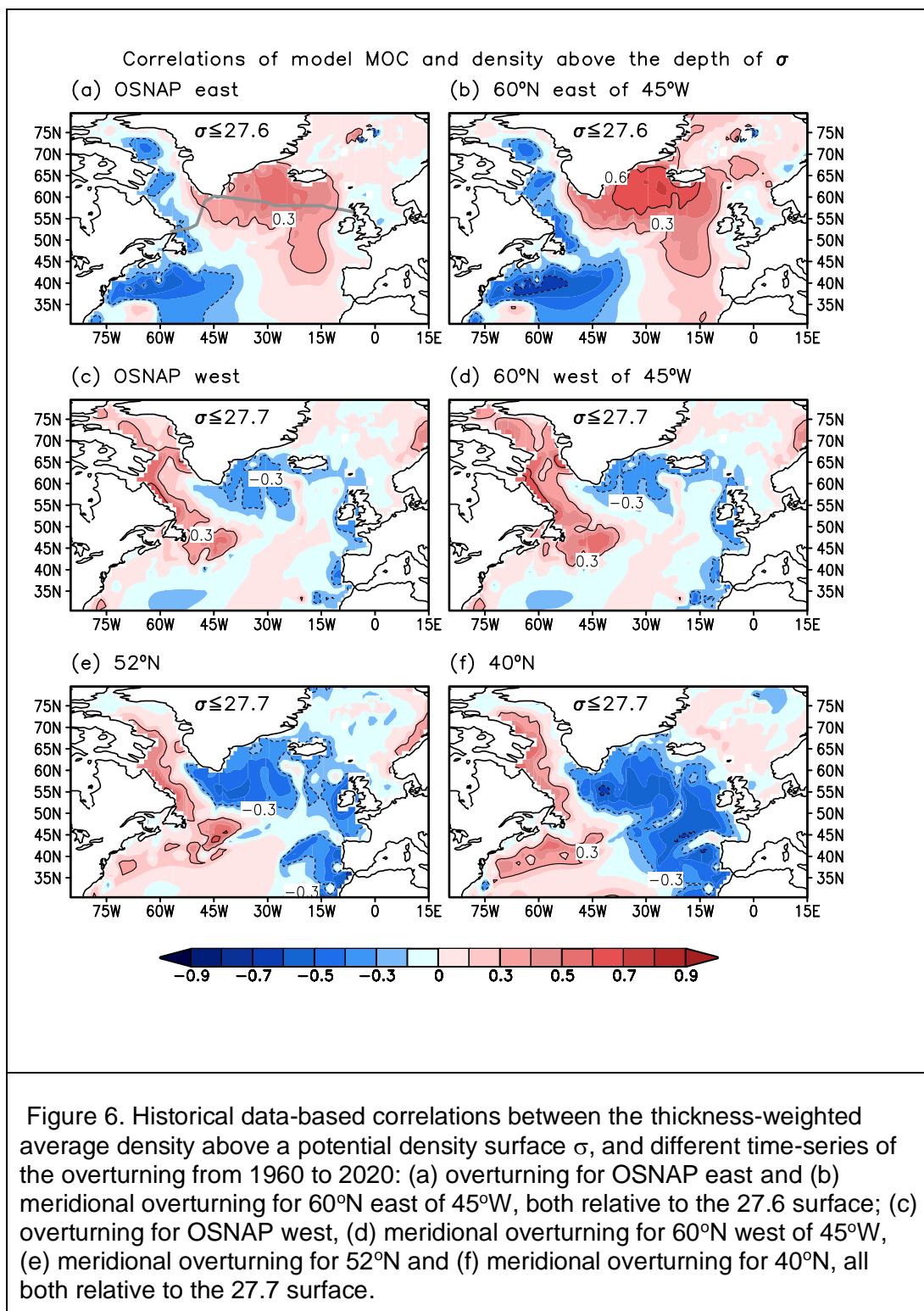
357 The overturning for OSNAP west is strongly correlated with the density above the $\sigma=27.7$ surface around
358 the Labrador Sea (reaching 0.62 at zero lag when including both end points of OSNAP west in Table 3).
359 The correlations reduce when including only a single end point of OSNAP west (Table 3), consistent with
360 the analysis of Li et al. (2021) for 4 years of monthly OSNAP data.

361 Maps of the correlation between the timeseries for the overturning for OSNAP west and the density above
362 the 27.7 surface reveal high correlations along the western side of the Labrador Sea, a similar pattern
363 occurs for the meridional overturning across the western side of 60°N (Fig. 6c,d). The meridional

364

overturning for 52°N and 40°N show similar correlation patterns to that of OSNAP west, revealing a positive correlation to the western boundary density (Fig. 6e,f).

365



366

367

2.6 Causality in the connections between the regional density and overturning

368

Understanding the causes of the correlations between regional density changes and the overturning,

369

especially in remote regions, needs further investigation. There may be a direct causal relationship when

370

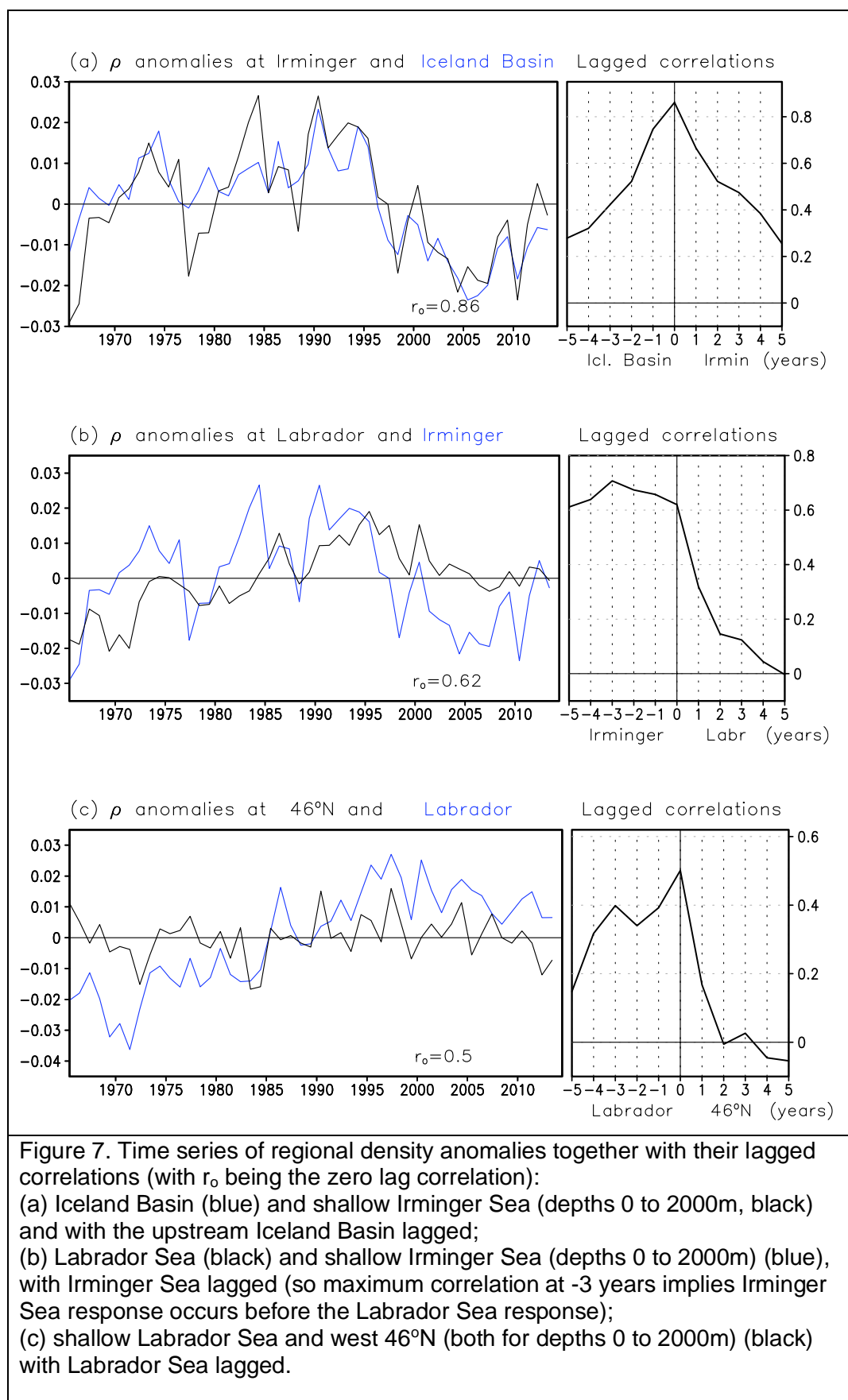
the local atmospheric forcing induces a boundary density anomaly which then generates an overturning

371 response. However, positive correlations between regional density changes in one region (such as the
372 Irminger Sea) and overturning over a wider region (such as the eastern basin) may arise because:
373 (i) the local boundary density changes may be influenced by upstream density changes, which are
374 communicated downstream, and the upstream density changes provide the actual control of the
375 overturning;
376 (ii) the local boundary density changes may be forced by large-scale atmospheric variability that also forces
377 boundary density, and hence overturning, changes elsewhere.

378 To gain insight into these possible connections, lagged correlations are evaluated for three different
379 combinations of time series of the regional densities, which are either upstream or downstream of Irminger
380 Sea and the Labrador Sea. First consider, the boundary density for the Irminger Sea (defined by a
381 shoreward region ranging from 0 to 2000m in depth, Fig. 2) and the upstream regional density anomaly in
382 the Iceland Basin, there is a strong correlation at zero lag of 0.86 (Fig. 7a). Both density anomalies are
383 probably responding to the same large-scale pattern in atmospheric forcing, although there is a possibility
384 of a rapid communication in less than a year between each region.

385 Second, for the boundary density anomalies of the Irminger Sea and the Labrador Sea, the changes in the
386 Irminger Sea precede the changes in the Labrador Sea with a maximum correlation of 0.7 with a 3 year lag
387 (Fig. 7b). This response is consistent with the boundary density in the Irminger Sea being advected along
388 the boundary to the Labrador Sea, as well as consistent with the recent modeling study of Menary et al.
389 (2020). This response is also consistent with the overturning for OSNAP east not being significantly
390 correlated with the density changes in the Labrador Sea at zero lag (Table 3).

391 Finally, for the boundary density changes of the Labrador Sea and further south on the western boundary
392 of the subpolar gyre at 46°N, there is a maximum correlation of 0.5 at zero lag together with a correlation of
393 0.4 at 3 year lag (Fig. 7c). This signal may then be due to a combination of a density response at zero lag
394 to coherent changes in atmospheric forcing together with a downstream communication of the Labrador
395 Sea density signals on a timescale of 3 years. Hence, the overturning for OSNAP west correlates with the
396 boundary density changes for the Labrador Sea and the meridional overturning at lower latitudes (Table 3),
397 involving the combined effects of coherent atmospheric forcing and boundary communication of density
398 anomalies.



402

403

404

405

406

Unravelling these competing effects of a local response to large-scale coherent patterns of atmospheric forcing and a communication and transport of density anomalies is challenging using the data-based reconstructions. Consequently, a series of forward model experiments (Section 3) are used next to reveal how regional density anomalies are formed and spread over the subpolar basin, and how they connect to

407 the overturning changes on the western and eastern sides of the basin, including whether those overturning
408 changes on each side of the basin are reinforcing or opposing each other.

410 **3 Forward-model experiments for the overturning response**

411 The aim is now to assess how regional density changes connect to the overturning changes across the
412 subpolar basin, and to separate the effects of a local versus upstream responses to atmospheric forcing.

413 *3.1 Methods*

414 Forward model experiments are conducted using the global MIT general circulation model (Marshall et al.,
415 1997) with a 1° grid with 23 vertical levels over the globe. The model is initialised from the climatological
416 temperatures and salinities and forced by the climatological monthly mean surface heat fluxes and wind-
417 stress from ECMWF reanalyses. In order to reduce the model drift, the sea-surface temperature (SST) is
418 relaxed to the climatological monthly mean SST on a timescale of 15 days during the first 50 years of the
419 spin-up. The virtual heat fluxes from the restoring term are diagnosed on monthly basis and combined with
420 the surface heat fluxes. This combined forcing is used for the rest of the spin-up with the SST relaxation
421 switched off. Due to the larger uncertainties in the freshwater fluxes, the use of explicit fluxes is avoided
422 and the sea-surface salinity is relaxed to the climatological monthly mean sea-surface salinity on a
423 timescale of 15 days. Monthly mean regional surface forcing anomalies are applied for a period of 10 years
424 after the initial 100 years spin-up. The regional forcing experiments employ surface forcing appropriate for
425 different composite states of the NAO (Fig. 8a) based on station data (Hurrell, 2013), consisting of 16
426 years for NAO+ and 12 years for NAO-. The model diagnostics are presented in terms of the difference
427 between the model experiment using the modified forcing and a model control using climatological forcing,
428 which minimises the effects of potential model drift. The modified forcing is taken from atmospheric
429 reanalyses by ECMWF for the appropriate years using ERA40 for 1960 to 1978 and ERA Interim for 1979
430 to 2020. The forward model experiments do not include any internal relaxation to the historical data, so do
431 contain model drift and systematic errors, such as including greater convection in the Labrador Sea and
432 larger changes in the overturning in OSNAP west than revealed in the data-based reconstructions.

433 The MOC along the OSNAP line from the forward control run is 15.7 Sv for OSNAP east and 7.0 Sv for
434 OSNAP west. The overturning for OSNAP east is in reasonable agreement with the data-based
435 reconstructions of 16.49 ± 0.62 Sv (Table 1). However, the overturning for OSNAP west is larger than the
436 data-based estimate of 3.42 ± 0.41 Sv. This larger value is typical for coarse-resolution models that are
437 unconstrained by observations, which may be due to overestimating deep convection in the Labrador Sea
438 and resulting changes in density distribution.

439 The modifications in the annual surface heat flux associated with the winter NAO typically reach ± 20 Wm^{-2} ,
440 providing enhanced cooling over much of the western subpolar gyre during NAO+ and less cooling during
441 NAO- (Fig. 8b,c). The large-scale coherence in the surface cooling anomaly for NAO+ leads to an
442 increase in the density for the upper 1300m over much of the subpolar gyre, particularly over the Labrador
443 Sea, the Irminger Sea and the Iceland Basin (Fig. 8d). The surface warming anomaly for NAO- instead

444
445
446

leads to a lightening over the western side of the subpolar gyre, particularly over the Labrador Sea and Irminger Sea (Fig. 8e).

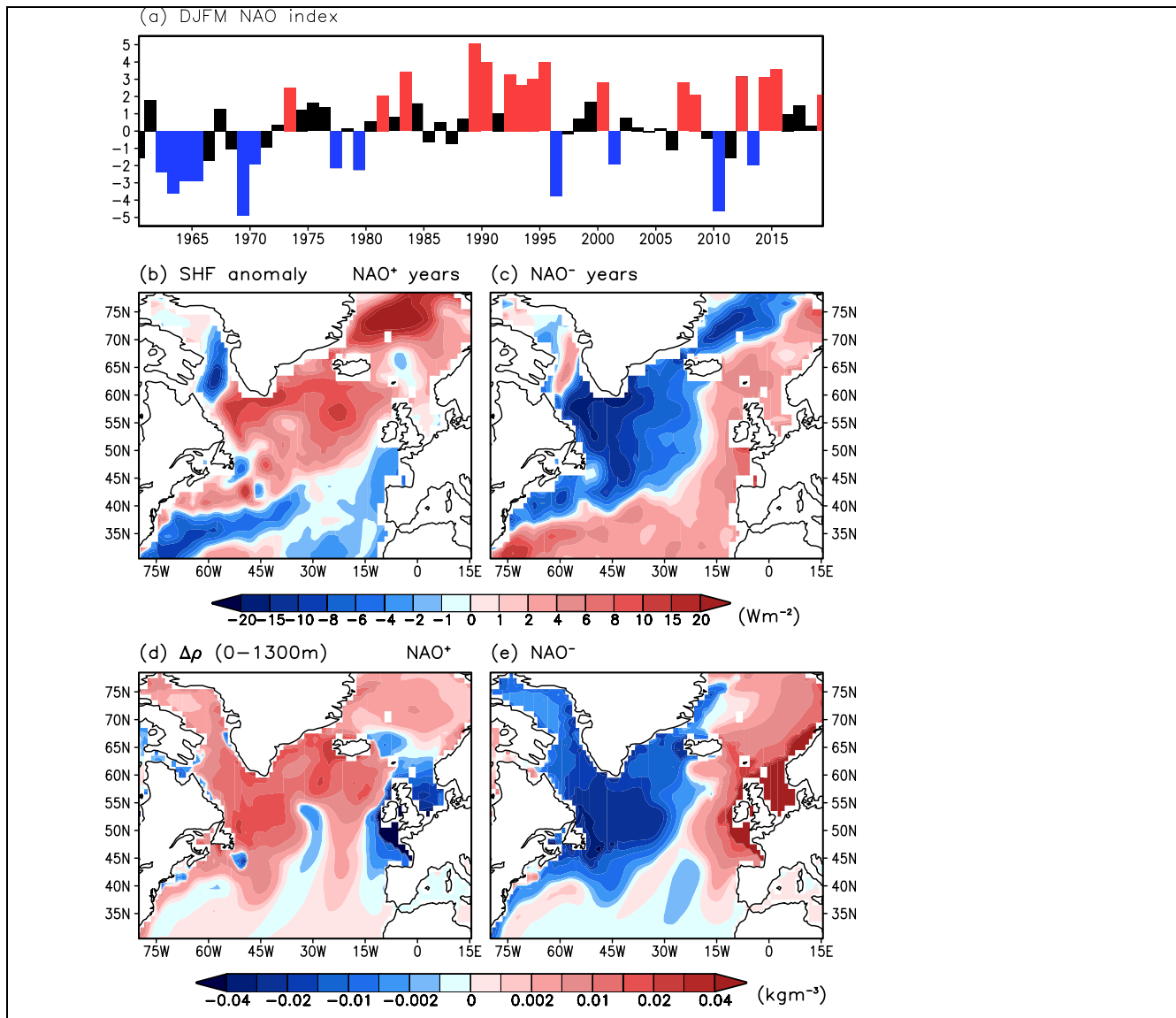


Figure 8. (a) winter NAO index based on December to March. The time record is separated into characteristic periods for NAO+ (red) and NAO- (blue) years; (b) NAO+ and (c) NAO- surface heat flux (SHF) anomalies from the ocean to the atmosphere for ECMWF for the years defined from (a); (d) NAO+ and (e) NAO- upper ocean density changes after 5 years of sustained NAO anomalies from only the surface heat flux.

447
448
449
450
451
452
453
454
455
456
457

For these forward experiments, the combined effect of changes in surface winds and surface heat fluxes linked to a NAO+ state leads to a strengthening in the overturning by 0.73 Sv for OSNAP west and 2.6 Sv for OSNAP east, while a NAO- state leads to a weakening in the overturning by -3.65 Sv for OSNAP west and -1.97 Sv for OSNAP east (Table 4). These overturning changes are the same sign as those diagnosed from the data-based reconstructions (Table 1), which for NAO+ state reach 0.44 Sv for OSNAP west and 1.12 Sv for OSNAP east, and for NAO- state reach -0.16 Sv for OSNAP west and -0.39 Sv for OSNAP east. Hence, for different states of the NAO, the overturning contributions have the same sign on both the western and eastern sides of the basin; this similarity in sign occurs in both our diagnostics of the data-based reconstructions and these forward model experiments when the forcing is applied to the entire basin.

Table 4. Forward model experiments for overturning changes (Sv) across OSNAP line after 5 years of sub-sampled NAO+/- forcing from ECMWF, which is either includes anomalous wind or buoyancy forcing or combined anomalies in wind and buoyancy forcing. Overturning is defined relative to the same maximum density limit, $\sigma_{max} = 27.8$, across the entire OSNAP line, so that the overturning across the full line is the sum of the OSNAP west and east contributions. In addition, the overturning change is included for historical data analysis (Table 1) for selected NAO+ and NAO- periods (Fig. 8a) with a lighter fixed density limit of $\sigma_{max} = 27.7$.

Forcing over entire domain	NAO+		NAO-	
	OSNAP west	OSNAP east	OSNAP west	OSNAP east
NAO winds	0.02	0.36	-0.19	-0.48
NAO buoyancy forcing	1.01	1.97	-3.44	-1.58
NAO winds + buoyancy forcing	0.73	2.60	-3.65	-1.97
Overturning change from historical data for $\sigma_{max} = 27.7$	0.44	1.12	-0.16	-0.39

459 This response is primarily controlled by the effects of the surface heat fluxes, since there are similar large
 460 responses if anomalous surface heat fluxes are imposed together with climatological winds: the overturning
 461 increases by 1.01 Sv for OSNAP west and 1.97 Sv for OSNAP east respectively, while the equivalent
 462 anomalous surface forcing for NAO- leads to a reduction in the overturning by -3.44 Sv for OSNAP west
 463 and -1.58 Sv for OSNAP east (Table 4). This stronger response for OSNAP west to NAO- forcing is due to
 464 larger anomalies in the surface heat flux in the western basin, as the overturning responses are similar in
 465 magnitude if the surface forcing anomaly is replaced by a spatially uniform $\pm 10 \text{ Wm}^{-2}$ (not shown). The
 466 overturning responses are in accord with the sign of the densification or lightening for the NAO+ and NAO-
 467 states (Fig. 8d,e). In contrast, there are much weaker responses if the surface forcing includes anomalous
 468 winds and climatological surface heat fluxes: the overturning only strengthens for NAO+ by 0.02 Sv for
 469 OSNAP west and 0.36 Sv for OSNAP east, while the overturning only weakens for NAO- by -0.19 Sv for
 470 OSNAP west and -0.48 Sv for OSNAP east. Hence, the buoyancy forcing is key to the pronounced
 471 changes in the subpolar overturning in our model experiments.

472 3.2 Overturning, density and circulation responses to localised regional forcing

473 Our aim is now to identify the effects of localised buoyancy forcing in controlling the overturning responses,
 474 so separating out the effect of a local response to density changes versus either far field density responses
 475 and/or the response to large-scale coherent patterns in atmospheric forcing. The subpolar domain is
 476 separated into 7 individual regions, including the Labrador Sea, the Irminger Sea and the Iceland Basin
 477 (Fig. 2). Separate modelling experiments are then performed where the NAO+ or NAO- surface buoyancy
 478 forcing is applied only to an individual region (Table 5). This process is repeated for each of the 7 individual

479 regions, so that the response to the buoyancy forcing over the entire domain may be viewed in terms of a
480 summation of the individual responses to the regional forcing.

481 For OSNAP west, the localised forcing for NAO+ and NAO- over the Labrador Sea and the Irminger Sea,
482 provide the dominant contribution to the overturning, accounting for 0.88 Sv and 0.59 Sv for NAO+ versus
483 -2.21 Sv and -0.98 Sv for NAO- respectively (Table 5).

484 For OSNAP east, the localised forcing over a broader region provides comparable contributions to the
485 change in the overturning: the forcing for NAO+ over the Irminger Sea, the Iceland Basin and the
486 southeast subpolar gyre account for 0.49 Sv, 0.81 Sv, and 0.38 Sv respectively; while the forcing for NAO-
487 over the Irminger Sea, the Iceland Basin, the southwest and southeast subpolar gyre account for -0.54 Sv,
488 -0.31 Sv, -0.33 Sv and -0.39 Sv (Table 5).

489

Table 5. Forward model regional experiments showing the overturning changes (Sv) after 5 years response to anomalous buoyancy forcing, where the forcing is either only applied to selected individual regions or for all of the regions combined together. The different regions are defined in Fig. 2. The buoyancy forcing is regionally sub-sampled for NAO+/- composite states based upon 16 years of NAO+ and 12 year of NAO- using a magnitude threshold of 1.8 with station data (Fig. 8a, red and blue) from ECMWF. Overturning is defined relative to the same density surface, $\sigma_{max} = 27.8$, across the entire OSNAP line, so that the overturning across the full line is the sum of the OSNAP west and east contributions.

Buoyancy forcing only over regional domain	NAO+		NAO-	
	OSNAP west	OSNAP east	OSNAP west	OSNAP east
Labrador Sea (LS)	0.88	-0.03	-2.21	0.04
Irminger Sea (IS)	0.59	0.49	-0.98	-0.54
Iceland Basin (IB)	-0.01	0.81	-0.12	-0.31
Southwest subpolar gyre (SW)	0.32	0.10	-0.69	-0.33
Southeast subpolar gyre (SE)	-0.11	0.38	-0.09	-0.39
European shelf (ES)	0.0	0.04	0.0	-0.15
Northeast and Norwegian Sea (NE)	0.01	0.06	-0.04	-0.01
All of the above forcing applied together	1.68	1.85	-4.13	-1.69

491 There are contrasting responses in terms of whether the overturning changes reinforce each other or
 492 oppose each other over the subpolar basin. For the Labrador Sea regional forcing case, the overturning
 493 response for OSNAP east is weak and the opposing sign of that for OSNAP west, while instead for the
 494 Irminger Sea regional forcing case, there are reinforcing contributions for OSNAP west and east. In order to
 495 understand these different responses, consider snapshots of the regional density response at years 1, 5
 496 and 10 after sustained patterns of the buoyancy forcing are applied after 100 years of initial spin up (Fig. 9
 497 with the anomalous forcing contained within the grey contour).

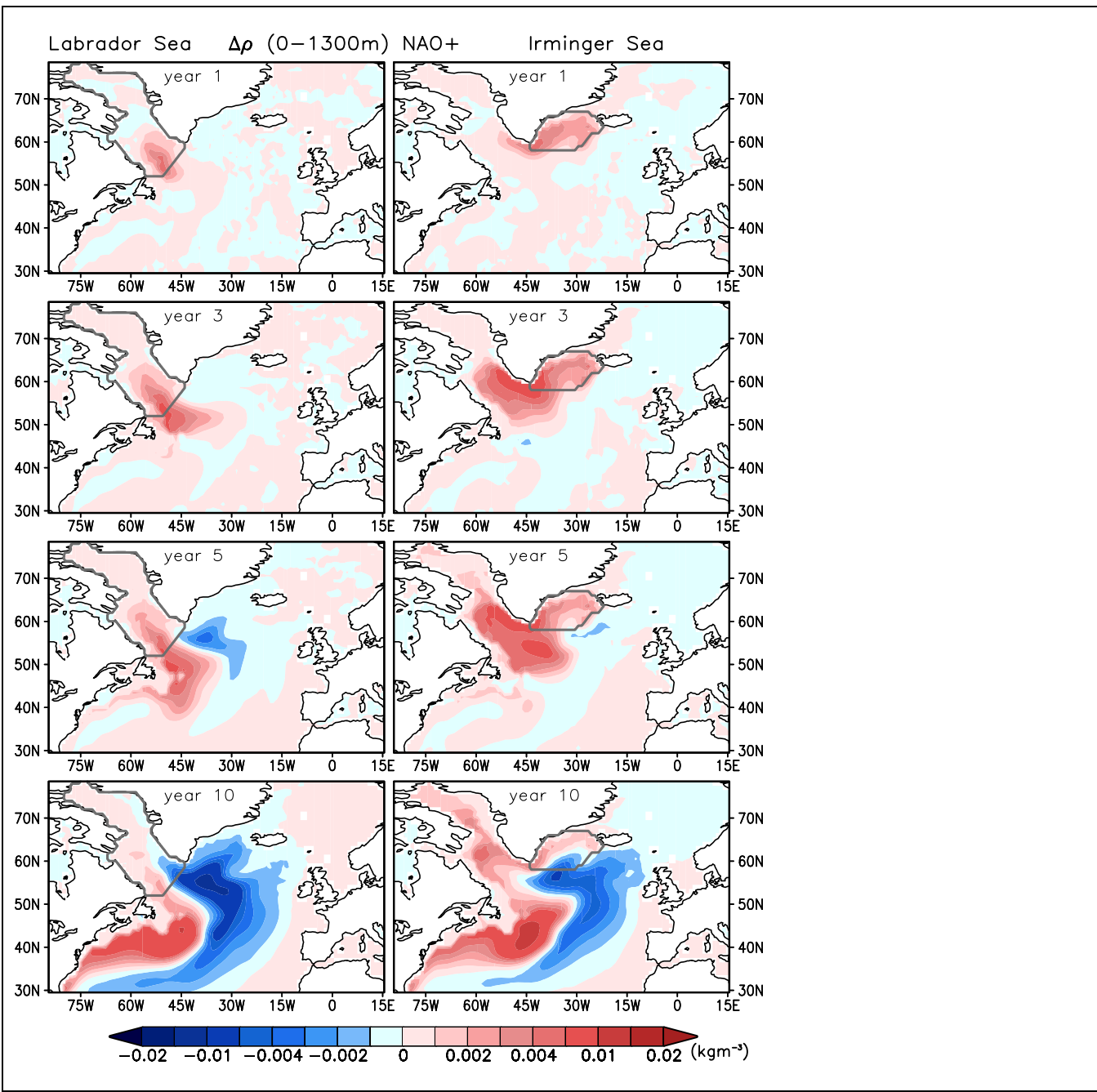


Figure 9. Regional experiments where NAO+ forcing is only applied for the Labrador Sea (left panel) or the Irminger Sea (right panel) using monthly mean surface heat anomalies from ECMWF subsampled NAO+. Density changes are shown after 1, 3, 5 and 10 years (after an initial spin up of 100 years).

499

500 For enhanced surface cooling for NAO+ applied only over the Labrador Sea, a positive density anomaly
 501 forms over the forcing region, which then spreads into the subpolar gyre and along the western boundary
 502 (Fig. 9, left panel). After 5 years, there is a dipole and a lighter anomaly is formed to the east of the dense
 503 anomaly. Crucially, there are opposing signs in the boundary density anomalies in the Labrador Sea and
 504 the Irminger Sea, which is consistent with there being opposing sign contributions for the overturning
 505 changes for OSNAP west and east (Table 5). There are similar responses with the opposing sign for NAO-
 506 (not shown).

507 For enhanced surface cooling for NAO+ applied only over the Irminger Sea, a positive density anomaly
 508 again forms over the forcing region, which then spreads along the western boundary into the Labrador Sea

509 (Fig. 9, right panel). After 5 to 10 years, there is again a dipole with a lighter anomaly to the southeast of
510 the dense anomaly. Crucially there are similar signs in the boundary density anomalies in the Labrador Sea
511 and the Irminger Sea, which is consistent with there being reinforcing sign contributions for the overturning
512 changes across OSNAP west and east (Table 5). There are similar responses with the opposing sign for
513 NAO- (not shown).

514 The dipole of positive and negative density anomalies is created through the effect of the direct forcing and
515 the resulting adjustment of the overturning circulation and horizontal transport (Fig. 10). For a formation of
516 denser fluid in the Labrador Sea (Fig. 9, left panel), there is a strengthening in the overturning and
517 meridional heat transport (Fig. 10a, left panel), enhancing the influx of warmer, lighter waters into the
518 northwestern part of the subpolar gyre, and reducing the strength of the boundary transport from the
519 Irminger Sea to Labrador Sea, and the transport from the Nordic Seas to the Irminger Sea (Fig. 10a, right
520 panel). Hence, the dense anomaly formed in the Labrador Sea is accompanied by a lighter boundary
521 density anomaly formed in the Irminger Sea. This dipole in boundary density is consistent with the opposing
522 sign contributions for the overturning changes for OSNAP west and east obtained in this experiment with
523 only local density forcing in the Labrador Sea (Table 5).

524 For the Irminger Sea case, the localised forcing associated with the NAO+ state leads to an increase in the
525 boundary density in the Irminger Sea and downstream similar changes in the Labrador Sea (Fig. 9, right
526 panel). There is an adjustment to the circulation involving a strengthening in the overturning again (Fig.
527 10b, left panel), but now the local density forcing leads to a strengthening in the transport from the Nordic
528 Seas to Irminger Sea and from the Irminger Sea to the Labrador Sea (Fig. 10b, right panel). The similar
529 signs in the boundary density changes in the Labrador Sea and Irminger Sea are consistent with the
530 similarly signed contributions for the overturning changes for OSNAP west and east.

531 Hence, the regional experiments suggest that a local forcing over the Labrador Sea does not provide the
532 similarly-signed overturning responses over the western and eastern sides of the subpolar basin, while the
533 regional forced experiments over the Irminger Sea provide overturning responses consistent with the data-
534 based reconstructions and the basin-wide forcing experiments (Tables 1, 4 and 5).

535

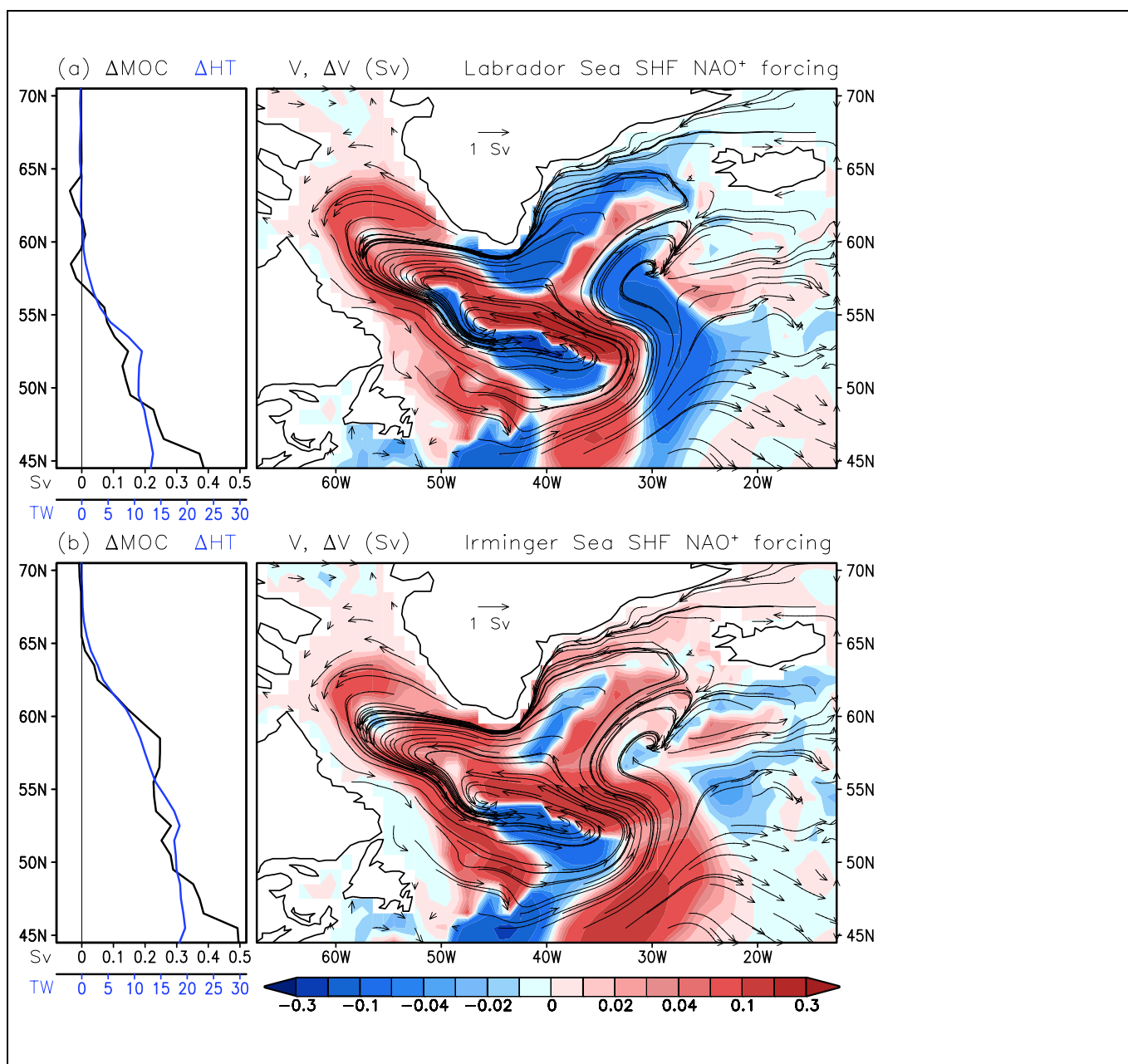


Figure 10. Change in the meridional overturning circulation (MOC, Sv, black) and the northward heat transport (HT, TW, blue) relative to control run with latitude (left panel) for 10 years of NAO+ surface heat flux (SHF) forcing localised in (a) Labrador Sea or (b) the Irminger Sea. In the right panels, the corresponding horizontal transport patterns over the upper 1300m for NAO+ are denoted by the vectors (black, Sv) together with changes in the strength of the horizontal transport for NAO+ minus the control (colours). For both cases, the density forcing increases the meridional overturning and enhances the northward heat transport (left panels), so acting to lighten the upper ocean. In (a), an increase in the density in the Labrador Sea with NAO+ forcing is associated with a strengthening in northwestern subpolar circulation enhancing the influx of warmer, lighter waters, as well as a reduced horizontal transport along the boundary from Irminger Sea to Labrador Sea. Conversely, in (b), an increase in the density in the Irminger Sea with NAO+ forcing is associated with a strengthening in the boundary transport from Irminger Sea to Labrador Sea, as well as from the Nordic Seas into Irminger Sea.

537 Given that there is a large-scale coherence to the atmospheric forcing of the subpolar basin, these regional
 538 experiments offer a cautionary note as to how basin-wide model experiments may be interpreted. The
 539 Labrador Sea density provides a useful metric for the overturning over the western side of the subpolar
 540 basin and at lower latitudes over the basin, as has been widely exploited in model studies (Delworth et al.,
 541 1993; Eden and Willebrand, 2001) and inferences from regional density changes (Robson et al., 2016).

542 However, in our regional experiments, a local forcing over the Labrador Sea acts to decrease the
543 overturning over the eastern side of the basin. Consequently, the Irminger Sea density provides a more
544 reliable metric of the overturning changes for the eastern basin.

545 **4 Discussion**

546 The relationship between the overturning of the subpolar North Atlantic and regional density is assessed
547 using a combination of historical, data-based reconstructions of the overturning over the last 60 years and
548 forward model regional experiments using buoyancy and wind forcing, characteristic of different states of
549 the North Atlantic Oscillation (NAO).

550 The data-based reconstructions are in accord with the Overturning in the Subpolar North Atlantic Program
551 (OSNAP) measurements of the subpolar overturning defined in density coordinates, which are dominated
552 by an eastern basin contribution between Greenland and Scotland (Lozier et al., 2019; Li et al., 2021). The
553 stronger overturning contribution for the eastern side of the basin is consistent with the larger west-east
554 boundary density contrast between Greenland and Scotland, compared with the weaker overturning
555 contribution and boundary density contrast from the western side of the Labrador Sea to the southern tip of
556 Greenland. In our reconstructions, the overturning for the eastern side of the basin is strongly correlated
557 with density changes over the Irminger Seas, while the overturning for the western side of the basin is only
558 strongly correlated with boundary density changes on the southwestern shelf of the Labrador Sea and the
559 southern tip of Greenland. In these density co-ordinates, the zonally-integrated geostrophic velocity along
560 potential density surfaces may be estimated from boundary contrasts in Montgomery potential, which are
561 determined by a combination of the density and sea surface height distributions.

562 There are caveats in the accuracy of the data-based reconstructions of the density with the uncertainty in
563 the density larger than the actual anomalies (Hodson et al., 2014) and differences in the magnitude of
564 density metrics according to the data source (Robson et al., 2014). These differences in density
565 reconstruction then lead to resulting differences in the reconstruction of the geostrophic component of the
566 overturning, as revealed in a comparison of 6 different data-based ocean analyses including the same
567 Hadley Centre product as used here (Karspek et al., 2015). While accepting these caveats, skillful
568 prediction of the overturning circulation in the North Atlantic basin still requires inclusion of these data-
569 constrained ocean reanalysis products for initialisation (Yeager et al., 2012; Robson et al., 2012, 2014b,
570 Matei et al., 2012).

571 To gain some insight into causal connections between the overturning and the regional density changes, a
572 suite of forward model experiments are conducted to separate out the effect of local and far-field responses
573 to the atmospheric forcing. The model experiments include anomalous atmospheric forcing for NAO+ and
574 NAO- states, but the anomalous forcing is only applied to a selected region, then this process is repeated
575 for 7 different regions making up the subpolar basin. In these experiments, a localised density increase
576 over the Irminger Sea increases the overturning over both the western and eastern sides of the basin due
577 to dense waters spreading to the Labrador Sea. This response is consistent with the Menary et al. (2020)
578 interpretation of Labrador Sea density changing due to upstream forcing in the Irminger Sea. Conversely, a
579 localised density increase over the Labrador Sea increases the overturning on the western side of the
580 basin, but decreases the overturning on the eastern side of the basin due to a greater influx of warmer,

581 lighter waters. These regionally-forced experiments then reveal that forcing over the Irminger Sea leads to
582 reinforcing western and eastern basin contributions to the overturning, which are consistent with our data-
583 based diagnostics of how the subpolar overturning responds to the NAO+ or NAO- forcing. In contrast, the
584 regional forcing experiments for the Labrador Sea lead only to an increase in the overturning for the
585 western basin.

586 Hence, the Irminger Sea density provides a useful metric for revealing whether there are likely to be
587 reinforcing overturning changes in the western and eastern sides of the subpolar basin, while the Labrador
588 Sea density provides a useful metric for the overturning for the western basin and lower latitudes of the
589 subpolar gyre. However, caution needs to be applied in interpreting any implied causality in these
590 relationships involving the Labrador Sea density and the overturning for the eastern basin, since this
591 connection is partly due to the coherent pattern of atmospheric forcing driving similar-signed density
592 changes over much of the basin and partly due to a communication and transport of density anomalies,
593 connecting upstream forcing to downstream responses.

594 **Acknowledgments**

595 VR and RGW acknowledge support from the UK Natural Environment Research Council NE/K010972/1
596 and NE/T013494/1. MSL acknowledges the support from the Physical Oceanography Program of the
597 National Science Foundation via Grant OCE-17-56223. NPH was supported by U.K. Natural Environment
598 Research Council National Capability program CLASS (NE/R015953/1), and NERC grants U.K. OSNAP
599 (NE/K010875/1 and NE/K010875/2) and U.K. OSNAP Decade (NE/T00858X/1). We thank Feili Li for
600 advice as to the correlations for the OSNAP timeseries. DS was supported by the Met Office Hadley Centre
601 Climate Programme funded by BEIS and Defra. We thank four referees for constructive comments that
602 strengthened the study.

603
604
605 **Availability of data.** The OSNAP array data from years 2014 to 2018 are available
606 at <http://hdl.handle.net/1853/63707> and www.o-snap.org. The annual-mean temperature and salinity data
607 from the Met Office statistical ocean reanalysis (Smith et al. 2015) and our data-based reconstructions of
608 the meridional overturning circulation are to be uploaded at [Zenodo.org](https://zenodo.org).

611 **References**

- 612 Baehr, J., Hirschi, J., Beismann, J. O., & Marotzke, J. (2004). Monitoring the meridional overturning
613 circulation in the North Atlantic: A model-based array design study. *Journal of Marine Research*, 62(3), 283-
614 312.
- 615
616 Bingham, R. J., Hughes, C. W., Roussenov, V., & Williams, R. G. (2007). Meridional coherence of the
617 North Atlantic meridional overturning circulation. *Geophysical Research Letters*, 34(23).

619 Bleck, R. and Smith, L.T., 1990. A wind-driven isopycnic coordinate model of the north and equatorial
620 Atlantic Ocean: 1. Model development and supporting experiments. *Journal of Geophysical Research:*
621 *Oceans*, 95(C3), pp.3273-3285.

622

623 Buckley, M. W. and Marshall, J. (2016). Observations, inferences, and mechanisms of Atlantic Meridional
624 Overturning Circulation variability: A review, *Rev. Geophys.*, 54, 5–63, doi:10.1002/2015RG000493.

625

626 Delworth, T., Manabe, S., & Stouffer, R. J. (1993). Interdecadal variations of the thermohaline circulation in
627 a coupled ocean-atmosphere model. *Journal of Climate*, 6(11), 1993-2011.

628

629 Eden, C., and Willebrand, J. (2001). Mechanism of interannual to decadal variability of the North Atlantic
630 circulation. *Journal of Climate*, 14(10), 2266-2280

631

632 Foukal, N. P. and Lozier, M. S. (2016). On the propagation of sea-surface temperature anomalies from the
633 subtropical gyre to the subpolar gyre in the North Atlantic. *Nature Communications*, doi:
634 10.1038/ncomms11333.

635

636 Gent, P. R., and McWilliams, J. C. (1990). Isopycnal Mixing in Ocean Circulation Models. *J. Phys.*
637 *Oceanogr.*, 20, no. 1: 150–55.

638

639 Greatbatch, R. J., Fanning, A. F., Goulding, A. D., & Levitus, S. (1991) A diagnosis of interpentadal
640 circulation changes in the North Atlantic. *J. Geophys. Res.*, 96, 22 009–22 023, doi:10.1029/91JC02423.

641

642 Hirschi, J., and Marotzke, J. (2007). Reconstructing the meridional overturning circulation from boundary
643 densities and the zonal wind stress. *Journal of Physical Oceanography*, 37(3), 743-763.

644

645 Hodson, D. L. R., Robson, J. I. and Sutton, R. T. (2014). An anatomy of the cooling of the North Atlantic
646 Ocean in the 1960s and 1970s. *Journal of Climate*, 27 (21). pp. 8229-8243. doi:10.1175/JCLI-D-14-
647 00301.1.

648

649 Holliday, N. P., Bacon, S., Cunningham, S. A., Gary, S. F., Karstensen, J., King, B. A., ... & McDonagh, E.
650 L. (2018). Subpolar North Atlantic overturning and gyre-scale circulation in the summers of 2014 and
651 2016. *Journal of Geophysical Research: Oceans*, 123(7), 4538-4559.

652

653 Hurrell, J. (2013). the National Center for Atmospheric Research staff. *The Climate Data Guide: Hurrell*
654 *North Atlantic Oscillation (NAO) Index (Station-Based)*.

655

656 Karspeck, A. R., D. Stammer, A. Kohl, G. Danabasoglu, M. Balmaseda, D. M. Smith, Y. Fujii, S. Zhang, B.
657 Giese, H. Tsujino, A. Rosati (2015). Comparison of the Atlantic Meridional Overturning Circulation between
658 1960 and 2007 in six ocean reanalysis products, *Climate Dynamics*, doi: 10.1007/s00382-015-2787-7

659

660 Li, F., Lozier, M. S., & Johns, W. E. (2017). Calculating the meridional volume, heat, and freshwater
661 transports from an observing system in the subpolar North Atlantic: Observing system simulation
662 experiment. *Journal of Atmospheric and Oceanic Technology*, 34(7), 1483-1500.

663

664 Li, F., Lozier, M. S., Danabasoglu, G., Holliday, N. P., Kwon, Y.-O., Romanou, A., Yeager, S. G., & Zhang,
665 R. (2019). Local and downstream relationships between Labrador Sea Water volume and North Atlantic
666 meridional overturning circulation variability. *Journal of Climate*, 32(13), 3883– 3898.

667

668 Li, F., Lozier, M. S., Bacon, S., Bower, A. S., Cunningham, S. A., de Jong, M. F., ... & Zhou, C. (2021).
669 Subpolar North Atlantic western boundary density anomalies and the Meridional Overturning
670 Circulation. *Nature Communications*, 12(1), 1-9.

671

672 Lozier, M.S., Roussenov, V., Reed, M. S. C., & Williams, R. G. (2010) Opposing decadal changes for the
673 North Atlantic meridional overturning circulation. *Nat. Geosci.*, 3, 728–734, doi:10.1038/ ngeo947.

674

675 Lozier, M. S., Bacon, S., Bower, A. S., Cunningham, S. A., De Jong, M. F., De Steur, L., ... & Zika, J. D.
676 (2017). Overturning in the Subpolar North Atlantic Program: A new international ocean observing
677 system. *Bulletin of the American Meteorological Society*, 98(4), 737-752.

678

679 Lozier, M. S., Li, F., Bacon, S., Bahr, F., Bower, A. S., Cunningham, S. A., ... & Zhao, J. (2019). A sea
680 change in our view of overturning in the subpolar North Atlantic. *Science*, 363(6426), 516-521.

681

682 Marotzke, J., Giering, R., Zhang, K. Q., Stammer, D., Hill, C., & Lee, T. (1999). Construction of the adjoint
683 MIT ocean general circulation model and application to Atlantic heat transport sensitivity. *Journal of*
684 *Geophysical Research: Oceans*, 104(C12), 29529-29547.

685

686 Marshall, J., Hill, C., Perelman, L., & Adcroft, A. (1997). Hydrostatic, quasi-hydrostatic, and nonhydrostatic
687 ocean modeling. *J. Geophys. Res.*, 102, 5733–5752, doi:10.1029/96JC02776

688

689 Matei D., Pohnmann H., Jungclas J., Müller W., Haak H., Marotzke J. (2012). Two tales of initializing
690 decadal climate prediction experiments with the ECHAM5/MPI-OM model. *J. Climate*, 25:8502–8522.

691

692 McCarthy, G. D., Brown, P. J., Flagg, C. N., Goni, G., Houpert, L., Hughes, C. W., ... & Smeed, D. A.
693 (2020). Sustainable observations of the AMOC: Methodology and technology. *Reviews of*
694 *Geophysics*, 58(1), e2019RG000654.

695

696 McDougall, T.J., Feistel, R., Millero, F.J., Jackett, D.R., Wright, D.G., King, B.A., Marion, G.M., Chen, C.,
697 Spitzer, P. and Seitz, S. (2009). The international thermodynamic equation of seawater 2010 (TEOS-10):

698 Calculation and use of thermodynamic properties. *Global ship-based repeat hydrography manual, IOCCP*
699 *report no, 14.*
700

701 McDougall, T.J. and Klocker, A. (2010). An approximate geostrophic streamfunction for use in density
702 surfaces. *Ocean Modelling*, 32(3-4), pp.105-117.
703

704 Mellor, G. L., Mechoso, C. R., & Keto, E. (1982). A diagnostic calculation of the general circulation of the
705 Atlantic Ocean. *Deep Sea Research Part A. Oceanographic Research Papers*, 29(10), 1171-1192.
706

707 Menary, M. B., Jackson, L. C., & Lozier, M. S. (2020). Reconciling the Relationship Between the AMOC
708 and Labrador Sea in OSNAP Observations and Climate Models. *Geophysical Research Letters*, 47(18),
709 e2020GL089793.
710

711 Montgomery, R.B. (1937). A suggested method for representing gradient flow in isentropic
712 surfaces. *Bulletin of the American Meteorological Society*, 18(6/7), pp.210-212.
713

714 Ortega, P., Robson, J., Sutton, R. T., & Andrews, M. B. (2017). Mechanisms of decadal variability in the
715 Labrador Sea and the wider North Atlantic in a high-resolution climate model. *Climate Dynamics*, 49(7),
716 2625-2647.
717

718 Robson, J., Hodson, D., Hawkins, E. D., & Sutton, R. (2014a). Atlantic overturning in decline?. *Nature*
719 *Geoscience*, 7(1), 2-3.
720

721 Robson, J., Ortega, P., & Sutton, R. (2016). A reversal of climatic trends in the North Atlantic since
722 2005. *Nature Geoscience*, 9(7), 513– 517.
723

724 Robson, J., Sutton, R., Lohmann, K., Smith, D., & Palmer, M. D. (2012). Causes of the rapid warming of the
725 North Atlantic Ocean in the mid-1990s. *Journal of Climate*, 25(12), 4116-4134.
726

727 Robson, J., Sutton, R., & Smith, D. (2014b). Decadal predictions of the cooling and freshening of the North
728 Atlantic in the 1960s and the role of ocean circulation. *Climate Dynamics*, 42(9), 2353-2365.
729

730 Smith, D. M., Allan, R. P., Coward, A. C., Eade, R., Hyder, P., Liu, C., ... & Scaife, A. A. (2015). Earth's
731 energy imbalance since 1960 in observations and CMIP5 models. *Geophys. Res. Lett.*, 42(4), 1205-1213.
732

733 Visbeck, M., Cullen, H., Krahnemann, G., & Naik, N. (1998). An ocean model's response to North Atlantic
734 Oscillation-like wind forcing. *Geophysical Research Letters*, 25(24), 4521-4524.
735

736 Williams, R. G., Roussenov, V., Smith, D., & Lozier, M. S., (2014). Decadal evolution of ocean thermal
737 anomalies in the North Atlantic: The effects of Ekman, overturning, and horizontal transport. *J. Climate*, 27,
738 698–719, doi:10.1175/JCLI-D-12-00234.1.

739

740 Williams, R. G., Roussenov, V., Lozier, M. S., & Smith, D. (2015). Mechanisms of heat content and
741 thermocline change in the subtropical and subpolar North Atlantic. *J. Climate*, 28(24), 9803-9815.

742

743 Yeager S., & Danabasoglu G. (2014) The origins of late-twentieth-century variations in the large-scale
744 North Atlantic circulation. *J. Climate*, 27(9):3222–3247.

745

746 Zou, S., Lozier, M.S. & Xu, X., 2020. Latitudinal Structure of the Meridional Overturning Circulation
747 Variability on interannual to decadal time scales in the North Atlantic Ocean. *Journal of Climate*, 33(9),
748 3845-3862. doi:10.1175/JCLI-D-19_0215.1.

749

750 **Appendix**

751

752 Historical data-based model reconstructions of the overturning in density space

753 The data-based reconstruction of the overturning are also evaluated relative to a constant maximum
754 density, $\sigma_{max} = 27.7$ surface in (1) (Fig. A1). For this definition, overturning across the full line equals the
755 sum of the overturning across the western section and the overturning across the eastern section. The
756 overturning across each individual section is less than or equal to the OSNAP definition of the maximum
757 overturning crossing the section.

758

759 **Figure A1**

760

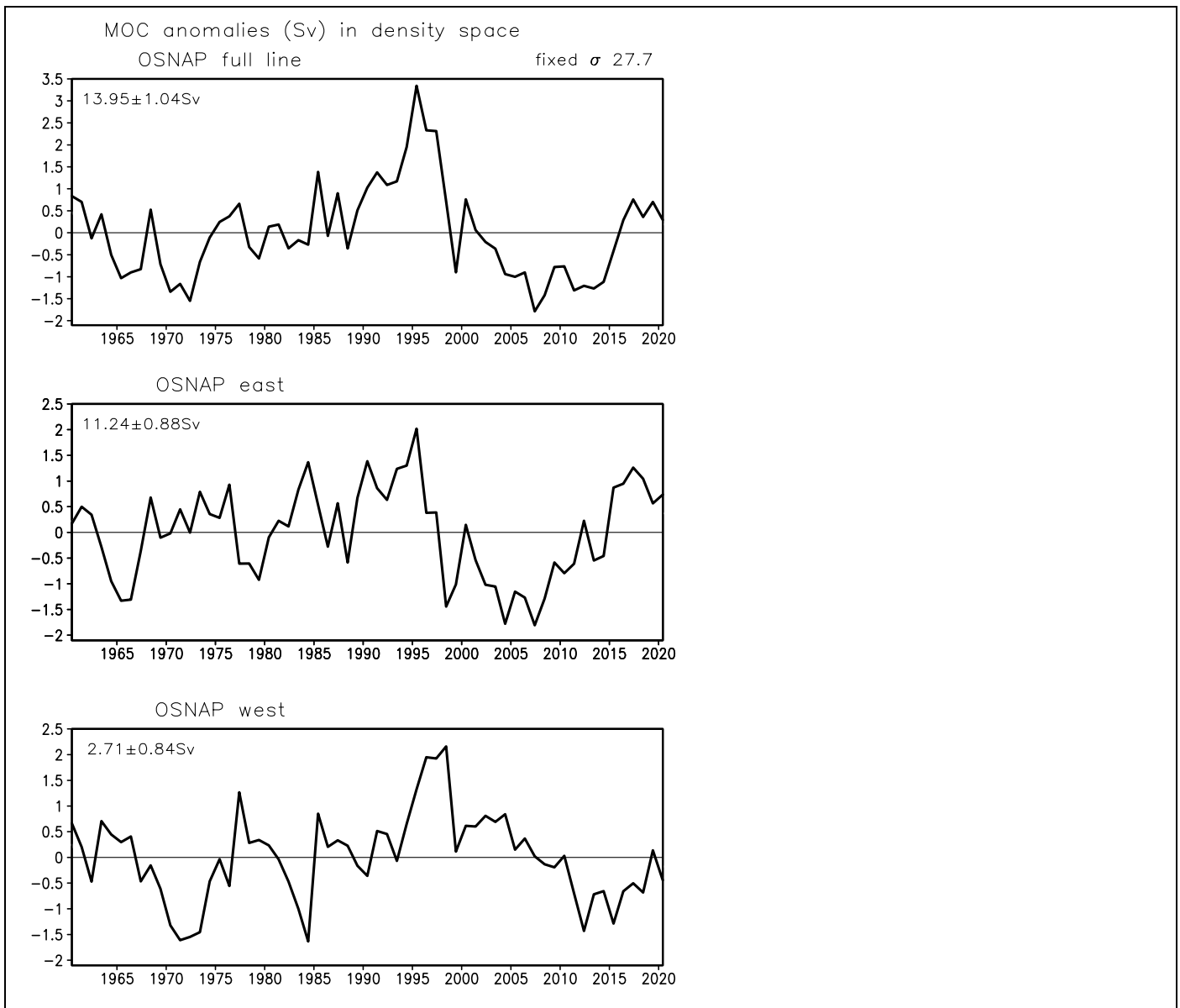
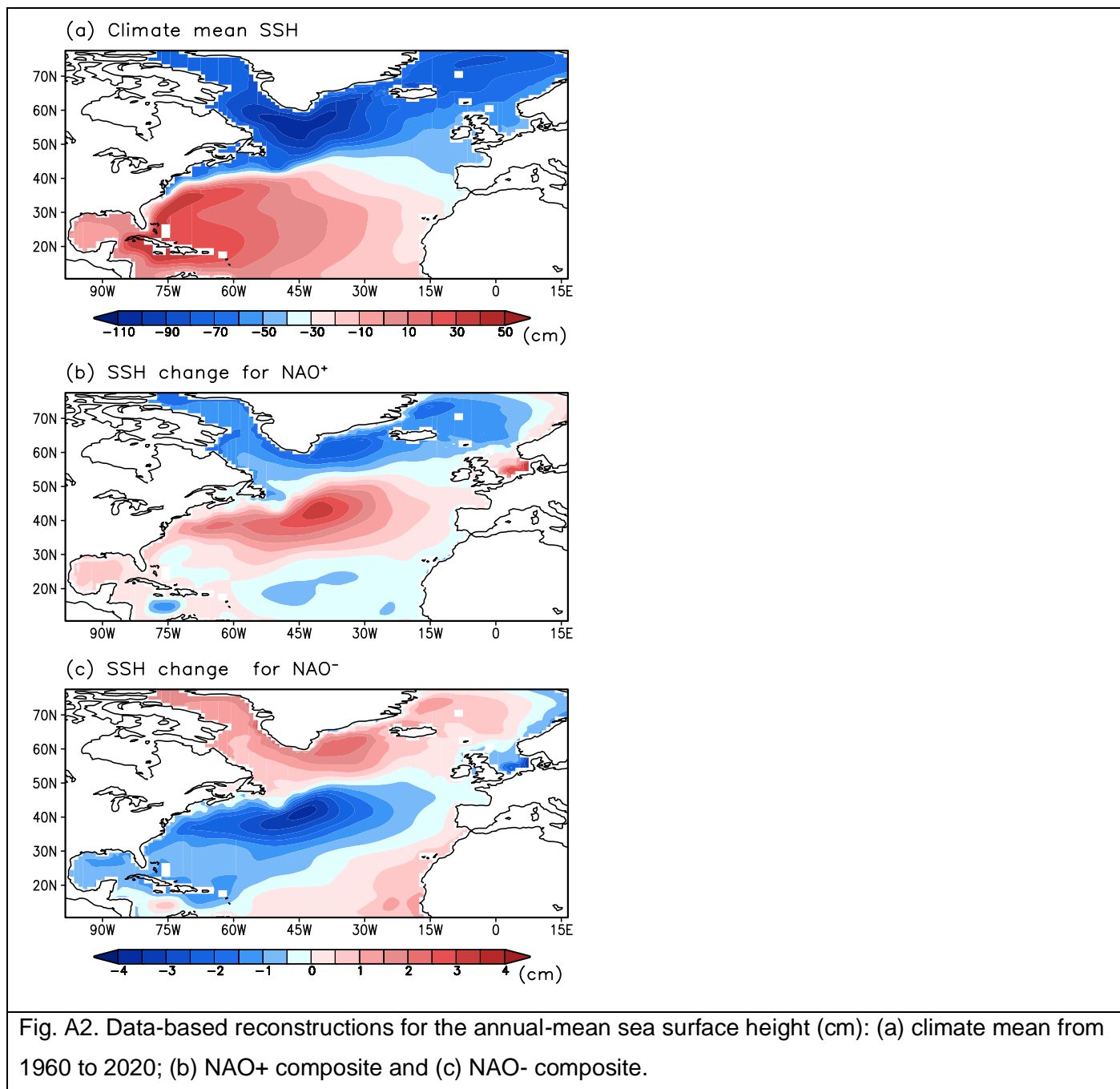


Fig. A1. Historical data-based model reconstructions of the overturning in density space (Sv) across the OSNAP full line from 1960 to 2020: (a) for the full line; (b) east of 45° W and (c) west of 45° W. Numbers show the long-term averages and standard deviations based on annual values. The overturning estimates are always defined relative to the same maximum density $\sigma_{max} = 27.7$ surface in (1). For this definition, overturning across the full line = the overturning across the western section + overturning across the eastern section.

761

762 The data-based reconstructions reveal subtropical and subpolar gyre circulations over the basin with sea
763 surface height changes reaching +50 cm over the subtropics and -110 cm in the subpolar gyre in the
764 climate mean from 1960 to 2020 (Fig. A2a). The pattern in the double gyre circulation is enhanced during a
765 NAO+ composite with sea surface height anomalies reaching magnitudes of 4 cm (Fig. A2b), and
766 conversely weakened for a NAO- composite (Fig. A2c).

767



768